Thermal Science and Engineering Progress 10 (2019) 10–26

Contents lists available at ScienceDirect

Thermal Science and Engineering Progress

journal homepage: www.elsevier.com/locate/tsep

Compressible Fanno flows in micro-channels: An enhanced quasi-2D numerical model for laminar flows

Marco Cavazzuti[a,*], Mauro A. Corticelli[b], Tassos G. Karayiannis[b]

[a] Dipartimento di Ingegneria "Enzo Ferrari", Università degli Studi di Modena e Reggio Emilia, Via P. Vivarelli 10, 41125 Modena, Italy
[b] Department of Mechanical and Aerospace Engineering, Brunel University London, Uxbridge, Middlesex UB8 3PH, United Kingdom

ARTICLE INFO

Keywords:
Compressible flow
Fanno flow
Micro-channels
Quasi-2D
Compressibility effects
Friction factor

ABSTRACT

Micro-scale fluid systems are becoming common in many applications ranging from electronic cooling to refrigeration systems and more. One-dimensional numerical models represent a simple and fast tool for the design of such devices, yet they struggle to accurately predict the flow characteristics in compressible micro-flows. Under the adiabatic assumption, the elegant theory developed by Fanno allows models for the viscous compressible flow in constant cross-section channels to be easily built. Although reasonably accurate, these models suffer from drawbacks inherent to their being one-dimensional, as such they cannot take into account the local profiles of quantities like the velocity and the temperature. In cascade, this results into incorrect evaluations of other dependent quantities, such as the dynamic pressure and the fluid thermophysical properties. The mismatch turns large when the fluid compressibility becomes important. As the Mach number grows, the velocity profile changes, and so the friction factor, even though a reliable model for predicting this change is still missing. In fact, a constant friction factor throughout the channel is generally assumed, following the incompressible flow theory. Here, a set of correlations is proposed improving the 1D theory accuracy by taking into account the effects of the non-uniform velocity and temperature profiles in a quasi-2D fashion. A detailed analysis of the velocity profiles at different Mach numbers coming from a large set of CFD simulations results in a model for assessing the impact of compressibility on friction and other quantities. The numerical model proposed, being able to properly account for the compressibility effects, offers an improved tool for the design of micro-scale fluid systems. Extending the analysis to include heat transfer is not difficult as the effect of heat flux will be analogous to the effect of pressure drop due to friction.

1. Introduction

The Fanno theory provides a differential model predicting the behaviour of non-isoentropic compressible flows in constant cross-section ducts due to friction, under the adiabatic assumption. This is a well-established model and represents an important extension of the classical theory of isoentropic compressible flows as found in most thermo and fluid dynamics textbooks [1]. The equations derived from this theory can be easily discretized and implemented into a one-dimensional numerical model, and offer reasonably accurate results of the flow characteristics for a given channel and boundary conditions. In a similar fashion, a model for computing the compressible isoentropic diabatic flow in constant cross-section channels also exists and is known by the name of Rayleigh theory.

The main applications where the Fanno flows are of interest relate to the gas flow in micro-channels. In fact, micro-flows are generally dominated by surface friction more than inertia, and are thus characterised by large total pressure drops, which translate into large streamwise flow accelerations generating even larger pressure drops. This motivates the interest in addressing the gas compressibility effects, which also affect heat transfer rates [2], when modelling these flows, since the Mach number and the fluid density change more and more rapidly while the sonic, or choked flow, condition is approached.

The interest in micro-flows in recent years was growing due to the miniaturization in many devices, and a number of interesting applications, ranging very different fields of investigation, can be found in the literature.

To cite a few examples, in [3] the two-phase flow in helically coiled capillary tubes as those used in the refrigeration industry was investigated experimentally and numerically. In [4] the flow in the mixing chamber of ejector refrigeration systems was modelled following the Fanno theory. A model for predicting the flow characteristics of an adiabatic capillary tube

* Corresponding author.
E-mail address: marco.cavazzuti@unimore.it (M. Cavazzuti).

https://doi.org/10.1016/j.tsep.2019.01.003

Nomenclature

a	JANAF coefficients
A	channel cross-section area
A_s	Sutherland coefficient
c	speed of sound
C	constant
c_p	heat capacity at constant pressure
D_h	channel hydraulic diameter
E	total energy
f	Darcy friction factor
F_v	viscous forces resultant
g	generic correction term/function
G	turbulence production term
h	specific enthalpy
H	channel height
k	turbulence kinetic energy
Kn	Knudsen number
L	channel length
$\dot{m}$	mass flow rate
Ma	Mach number
p	pressure
Po	Poiseuille number
r	radial coordinate
R	channel radius
R_g	specific gas constant
Re	Reynolds number
t	generic parameter
T	temperature
T_s	Sutherland temperature
U	velocity
U^+	dimensionless velocity
U_τ	friction velocity
W	channel width
x	longitudinal coordinate
y	heightwise coordinate
y^+	wall coordinate
Y	turbulence dissipation rate
z	widthwise coordinate
Z	turbulence cross-diffusion term

Greek symbols

α	channel aspect ratio (= L/D_h)
β	rectangular cross-section aspect ratio (<1)
γ	heat capacity ratio
Γ	effective diffusivity
Δ	difference
η	annular cross-section radii ratio (= R_i/R_o)
κ	Von Karman constant
μ	dynamic viscosity
ν	kinematic viscosity
ρ	density
τ	stress tensor
τ_w	wall shear stress
ω	turbulence specific dissipation rate

Subscripts

0	upstream stagnation value
1	downstream stagnation value
avg	area-weighted average
ax	axial
blk	mass-weighted average
c	relative to the channel centre
d	dynamic
eff	effective
i	inner
inc	incompressible
max	maximum
o	outer
out	relative to the outlet section
rad	radial
ref	reference value
t	total

Superscripts

[i]	generic element of the discretization

in a transcritical CO_2 heat pump system was discussed in [5], while friction in supercritical CO_2 flows for a nuclear reactor application was addressed in [6]. Fanno flow models were also applied in [7] for modelling the blow off lines of axial gas turbines, in [8] where the leakages in damaged distribution pipelines were modelled as real gas compressible flows, and in [9] where a model for circular porous air bearings was presented. A synoptic table resuming the fields of applications, together with the channel dimensions and the flow regimes encountered in the referenced works is given in Table 1 as a summary. As shown the flows are mostly turbulent when the hydraulic diameter is in the range of millimeters, while it becomes mostly laminar as the channel size is reduced.

Regarding the theoretical background, the Fanno model is based on a set of three first-order differential equations, representing the conservation of mass, momentum, and energy, and a constitutive equation given by the ideal gas law. Three boundary conditions are thus needed in order to solve the flow in a channel. Typically these are the upstream

Table 1
Synoptic table of possible micro-flow applications according to the referenced literature.

Author	Application	Fluid	Hydraulic Diameter	Length	Flow Regime
Deodhar et al. [3]	Refrigeration systems	R134a	0.9–1.1 mm	1.3–2.0 mm	Turbulent
Agrawal and Bhattacharyya [5]	Heat pumps	CO_2	1.0–1.3 mm	1.5–2.0 m	Turbulent
Mignot et al. [6]	Sodium reactors	CO_2	2–7 mm	33–34 cm	Turbulent
Plante et al. [9]	Porous air bearings	Air	2–38 μm	5 mm	Laminar
Shiraishi et al. [10]	Pneumatic pipeline	Air	2–4 mm	2–3 m	Turbulent
Kawashima and Asako [11]	MEMS	N_2	40–400 μm	14–150 mm	Lam./Turb.
Kohl et al. [12]	MEMS	Air/Water	25–100 μm	10–22 mm	Lam./Turb.
Asako et al. [13]	Generic	Air	20–200 μm	0.5–10 mm	Laminar
Hong et al. [14]	MEMS	N_2	146–203 μm	27 mm	Lam./Turb.
Cavazzuti and Corticelli [15]	Vents for moulding	Air	40–500 μm	1–25 cm	Lam./Turb.

and the downstream stagnation pressures, and the stagnation temperature. A set of equations linking the variations of the quantities of interest, such as pressure, temperature, and velocity, to the local Mach number and friction factor can be derived. The solution of the flow in the channel is thus found iteratively by searching for the inlet Mach number that allows the outlet boundary condition imposed to be met.

Several works in the literature investigate the compressible flow in micro-channels from a theoretical point of view, either focusing on particular flow cases, or proposing extensions to the basic theory. For instance, [16] concentrates on cases where the ideal gas assumption does not hold by providing solutions for different real steam state equations, while in [17] the dense real gas condition was investigated, a particular state where the choking condition may not be attained due to the velocity with which the fluid properties change with temperature and pressure in a real gas. In [18] the rarefied gas flow in non-homogeneous roughness channels was considered, a typical situation where the Knudsen number tends to be high (*e.g.*, $\mathrm{Kn} \geqslant 10^{-3}$) and the continuum hypothesis starts to break down. A portion of the literature also deals with multi-phase micro-channel boiling flows such as in [19] where the onset of flow oscillations and instabilities are investigated.

In [20] an extension of the Fanno theory for solving the variable cross-section channel case was given, yet this requires an additional function relating the change in pressure to the change in area, which in general is not known *a priori*. In [21] and in [10] direct approximate solutions of the Fanno flow are proposed; these are made possible if a uniform friction factor throughout the channel is assumed. The latter work also discusses how to best guess this reference friction, knowing that in reality this factor is far from uniform. A closed form solution of the Fanno problem was sought in [22], limitedly to the mass flow rate, under the assumption of subsonic flow in circular cross-section channels. In [23], Fanno and Rayleigh theories are used to create an unsteady 1D numerical model used to investigate the shock wave propagation and attenuation in long narrow tubes. It is interesting to note how the great majority of the works in the literature addresses flows that are at most moderately compressible. Mach numbers above 0.6, in fact, are very seldomly met. This shows that a comprehensive model to properly account for the effects of compressibility in micro-flows is still missing.

The experimental study of compressible flows in micro-channels poses a number of issues, discussed in detail in [2,24]. First of all there are serious difficulties in having a strict control, due to technological limits, over the channel dimension, shape, and relative roughness as the size of the channel reaches the micro scale. Secondly, still due to the scale of the problem, it is very difficult to collect accurate measurements, and this is particularly true for temperature, as explained in [11]. As a consequence, a reliable prediction of the friction factor based on experiments is almost impossible. This gave rise to several works questioning the applicability of the traditional formulas of fluid dynamics to the case of micro-flows, and where the discovery of completely different micro-scale fluid effects was erroneously hypothesized.

Even though it is true that the traditional formulas are no longer applicable when the Knudsen number is high, this is often not the case at the micro-scale unless the gas is very rarefied, and in the literature it is now accepted that fluid dynamics does not need to be fully rewritten to be applied to micro-flows, even though it may need some extensions to be addressed with care. In [25] and in [12] the deviations encountered in the previous works are ascribed to errors and uncertainties in the measurements which are extremely likely to happen for the reasons stressed above. The latter work also focuses on the correct way to proceed in an experimental campaign in order to control the sources of error at best.

In the understanding of compressible flows, three main challenges are still identified in the literature, these are:

- Entrance effects
  As the flow enters the channel its velocity profile is far from developed causing an extra friction in the entrance region. The extension of this region may vary, but in general the entrance effects diminish rather quickly so that they and are no longer noticeable after a distance of 20 to 50 hydraulic diameters from the inlet section. When the channel aspect ratio is high, *e.g.* $\alpha = L/D_h > 300$ according to [12], the entrance effects can be neglected, otherwise they affect the flow characteristics to some extent even though their impact is generally of secondary importance. To the authors' knowledge, some works on developing flows were discussed in [26] but no general model for the assessment of the velocity profiles and of the friction factors in the entrance region of a pipe still exist in the literature, in particular for compressible flows.
- Slip wall effects
  In the numerical models the no-slip wall boundary condition is typically enforced in the momentum equation. Similarly, the no-temperature-jump wall boundary condition is imposed in the energy equation. These are valid as long as the mean free path is much smaller than the characteristic length of the problem, that is to say when the Knudsen number is small (*e.g.*, $\mathrm{Kn} \leqslant 10^{-3}$). If this is not the case, a certain degree of tangential velocity slip should be taken into account for accurate results [27] altering the velocity gradients and profiles in the pipe. Some models exist for taking the slip wall effects into account [28], even though there is still work to be done on the topic. In micro-flows these effects are seldomly of interest as the Knudsen number is generally small, while they become important at the nano-scale.
- Compressibility effects
  In compressible flows in micro-channels the velocity profiles are always changing due to the quick flow acceleration. The transverse velocity component is not null, and tends to flatten the profile as the Mach number grows. As a consequence, the velocity gradient at the channel wall grows, and the same happens to the wall shear stress and the friction factor. This phenomenon becomes particularly evident for $\mathrm{Ma} > 0.3$, so that the flow cannot be treated as incompressible anymore. A few attempts have been made in the literature to correlate the compressible friction factor to the local Mach number, but only for moderate Mach numbers, as discussed in [13] and in [14]. This topic is still scarcely addressed, and a deeper understanding of the characteristics of compressible fluid flows could hopefully lead to more accurate correlations for friction factor and heat transfer rates [29] over larger operating conditions.

These three aspects are commonly disregarded in the numerical models, while their predictive capability could be greatly enhanced if they could be understood and modelled more in detail. This is particularly true for the latter which represents the core of the present work.

In a previous work [15] the authors presented a numerical model for solving the Fanno flow of an ideal gas. The model included temperature-dependent thermodynamic properties, and implemented two CFD-based correlations for the compressible friction factor in function of the Mach number: one for the case of laminar flow, the other for the turbulent flow. The correlation coefficients in the model were calibrated in order to minimize the mean absolute percent error over a sampling of the results from 80 CFD simulations. The model returned reasonably good results with a mean error $< 0.75\%$ over the mass flow rate prediction.

In the present work the Fanno-based model prediction capability is further improved with respect to some of the most critical issues previously noted. Due to the vastity of the argument only the case of laminar flow is addressed here, yet this is the most interesting case since turbulent flow conditions are rarely encountered in micro-channels.

At first, considering the Hagen-Poiseuille law for laminar incompressible flows, a precise assessment of the local average dynamic pressure, bulk temperature, and friction factor are analytically derived from the actual parabolic velocity profile over different cross-section types. The local dynamic pressure and temperature, in fact, whether the

flow is compressible or not, depend on the local velocity profile, and the single average velocity value available from the one-dimensional model is not sufficient for the proper assessment of these quantities on a section of the channel. This is particularly evident when the Mach number is high, and non-negligible errors are seen to propagate to all the quantities of interest computed using the Fanno equations, from pressures, to temperatures, densities, and the other thermophysical properties of the gas. The same holds for the friction factor, as it depends on the velocity gradient at the wall. In view of this, proper coefficients improving the one-dimensional model prediction capabilities are introduced and discussed. These coefficients come from the analysis of the velocity profiles, providing the model with quasi-2D accuracy.

Secondly, with the aid of a large set of CFD simulations, the results previously found for the incompressible flow case are confirmed, and numerically extended into a set of compressible flow correlations in function of the Mach number. Once again the correlations come from a detailed analysis of the velocity profiles in micro-channels, focusing on the changes induced by compressibility with respect to what is predicted by the Poiseuille law. Both the circular and the parallel-plates cross-section cases are investigated.

The approach followed and the correlations proposed are proven to be more rigorous and accurate compared to the one in the previous work from the authors where correlations were presented for the friction factor alone and were calibrated in order to better match a set of generic results, both global and local, extracted from the CFD simulations. The analysis of the velocity profiles at several locations also allows a novel and deeper insight over the issue of compressibility, and a net separation between the entrance effects, which are not investigated in this study, and the compressibility effects.

2. Theoretical background

The theoretical background of Fanno flows is briefly recalled here. A more extended treatment is reported in [15], while detailed analyses can be found in specialised textbooks [30].

From the conservation equations, the ideal gas state equation, and the definitions of the Mach number and of the speed of sound for a gas, five differential forms can be derived from which the main thermodynamic quantities can be computed. These are: pressure, temperature, density, velocity, and the Mach number.

From the definition of the Mach number and of the speed of sound, and by differentiating, we have

$$\mathrm{Ma} = \frac{U}{c}, \quad c = \sqrt{\gamma R_g T} \quad \Rightarrow \quad \frac{1}{2}\frac{\mathrm{d}T}{T} + \frac{\mathrm{dMa}}{\mathrm{Ma}} = \frac{\mathrm{d}U}{U}, \tag{1}$$

while from the equation of state

$$p = \rho R_g T \quad \Rightarrow \quad \frac{\mathrm{d}p}{p} = \frac{\mathrm{d}T}{T} + \frac{\mathrm{d}\rho}{\rho}. \tag{2}$$

From the continuity equation

$$\dot{m} = \rho U A \quad \Rightarrow \quad \frac{\mathrm{d}\rho}{\rho} = -\frac{\mathrm{d}U}{U}, \tag{3}$$

while from the energy conservation equation

$$c_p T + \frac{U^2}{2} = h_0 \quad \Rightarrow \quad \frac{\mathrm{d}T}{T} = (1-\gamma)\mathrm{Ma}^2\frac{\mathrm{d}U}{U}. \tag{4}$$

Finally, from the momentum conservation equation

$$F_v = \Delta(p + \rho U^2)A \quad \Rightarrow \quad \frac{\mathrm{d}p}{\rho U^2} + \frac{\mathrm{d}U}{U} = -\frac{1}{2}\frac{f\mathrm{d}x}{D_h}, \tag{5}$$

where F_v is the resultant of the viscous forces, and f is the Darcy friction factor. By substituting Eq. (5) in the previous ones, the five differentials $\mathrm{d}p/p$, $\mathrm{d}T/T$, $\mathrm{d}\rho/\rho$, $\mathrm{d}U/U$, and dMa/Ma can be expressed in function of the Mach number and of the quantity $f\mathrm{d}x/D_h$:

$$\begin{cases} \frac{\mathrm{d}p}{p} = \frac{-\gamma\mathrm{Ma}^2[1+(\gamma-1)\mathrm{Ma}^2]}{2(1-\mathrm{Ma}^2)}\frac{f\mathrm{d}x}{D_h} \\ \frac{\mathrm{d}T}{T} = \frac{-\gamma(\gamma-1)\mathrm{Ma}^4}{2(1-\mathrm{Ma}^2)}\frac{f\mathrm{d}x}{D_h} \\ \frac{\mathrm{d}\rho}{\rho} = \frac{-\gamma\mathrm{Ma}^2}{2(1-\mathrm{Ma}^2)}\frac{f\mathrm{d}x}{D_h} \\ \frac{\mathrm{d}U}{U} = \frac{\gamma\mathrm{Ma}^2}{2(1-\mathrm{Ma}^2)}\frac{f\mathrm{d}x}{D_h} \\ \frac{\mathrm{dMa}}{\mathrm{Ma}} = \frac{\gamma\mathrm{Ma}^2\left(1+\frac{\gamma-1}{2}\mathrm{Ma}^2\right)}{2(1-\mathrm{Ma}^2)}\frac{f\mathrm{d}x}{D_h}. \end{cases} \tag{6}$$

These equations are at the basis of the one-dimensional numerical model. The other quantities of interest are derived algebraically from their definitions. These are: the speed of sound c, the heat capacity c_p and the heat capacity ratio γ, the dynamic viscosity μ, the total pressure p_t, and finally the Reynolds Re and the Knudsen Kn numbers.

The importance of the correct assessment of friction is thus evident as this quantity plays a fundamental role in the governing equations. However, although having the great merit of providing expressions relating all the quantities to friction, the Fanno theory does not provide a tool for the determination of friction. This must be sought in the traditional formulas of fluid dynamics, which yet only provide a solution for the incompressible flow case.

3. Numerical model

The Fanno flow governing equations, Eqs. (1)–(5), have been implemented in a one-dimensional numerical model of a micro-channel. The domain is discretized in a number of segments, and the equations are solved sequentially for each element. A simple explicit forward first-order Euler method in space has been deemed sufficient for an accurate solution of the Fanno flow differential equations: using a number of elements in the range between 10^3 and 10^4 the flow is solved on average in just a few seconds of CPU time on an ordinary PC, and the CPU time required scales linearly with the number of elements.

The solution should not be based on Eq. (6) since the friction factor is not constant along the channel. It is preferred to evaluate explicitly the Mach number from the differential form in Eq. (6), renamed below as Eq. (7).

$$\frac{\mathrm{dMa}}{\mathrm{Ma}} = \frac{\gamma\mathrm{Ma}^2\left(1+\frac{\gamma-1}{2}\mathrm{Ma}^2\right)}{2(1-\mathrm{Ma}^2)}\frac{f\mathrm{d}x}{D_h}, \tag{7}$$

and use the Mach number thus found to iteratively solve the i-th element by using Eqs. (1)–(5) in a different form where f does not appear explicitly:

$$\begin{cases} U^{[i]} = \frac{\dot{m}}{\rho^{[i]}A} \\ T^{[i]} = T_0 - g\frac{U^{2[i]}}{2c_p} \\ p^{[i]} = p^{[i-1]}\frac{\mathrm{Ma}^{[i-1]}}{\mathrm{Ma}^{[i]}}\sqrt{\frac{T^{[i]}}{T^{[i-1]}}} \\ \rho^{[i]} = \frac{p^{[i]}}{R_g T^{[i]}} \\ \mathrm{Ma}^{[i]} = \frac{U^{[i]}}{c}. \end{cases} \tag{8}$$

The fluid properties c_p and c are also updated iteratively as function of the temperature according to their definitions. This internal iterative procedure usually converges in just a few iterations allowing more strict control over the residuals. The boundary conditions required for solving the system are the stagnation temperature T_0, the upstream stagnation pressure p_0, and the downstream stagnation pressure p_1. In Eq. (8) the mass flow rate $\dot{m}$ is known from the boundary conditions and the inlet Mach number, while g is a factor for the proper evaluation of the dynamic component of temperature as will be discussed below.

Due to the nature of Eq. (7) the system can only be solved if the Mach number at some point along the channel is known. For this reason

the set of equations is solved iteratively, where the inlet Mach number is guessed with a shooting technique up to when, for given upstream boundary conditions, the downstream boundary condition is met.

The iterative procedure starts from a low Mach number and increase it step by step up to when either the predicted downstream stagnation pressure is lower than the boundary condition p_1, or the sonic condition is exceeded at the channel outlet. From there we proceed backwards with a bifurcation method up to when either the p_1 boundary condition or the sonic outlet condition are met within a given tolerance (namely, $\Delta p \leqslant 0.1$ Pa or $\Delta \mathrm{Ma} \leqslant 10^{-5}$ from below). We refer to these conditions as the p and the Ma stopping criteria, respectively. When the p stopping criterion is met the shooting technique generally converges within a few tens of iterations, while when the Ma criterion is met up to one or two hundreds may be required.

As the fluid temperature can change quite significantly with the Mach number, it is deemed important to evaluate the thermophysical properties as accurately as possible in function of the temperature. For this reason, the dynamic viscosity μ is computed following the two-coefficients Sutherland law, [31],

$$\mu = A_s \frac{\sqrt{T}}{1 + T_s/T}, \tag{9}$$

and the specific heat c_p from the polynomial law using the JANAF coefficients, [32]

$$c_p = (a_0 + a_1 T + a_2 T^2 + a_3 T^3 + a_4 T^4) R_g. \tag{10}$$

The coefficients were computed in order to grant a good interpolation of the thermal properties up to a temperature of 1000 K for air as a working fluid: $A_s = 1.5072 \times 10^{-6}$ kg/m s $\mathrm{K}^{1/2}$, $T_s = 123.37$ K, $a_0 = 3.735856$, $a_1 = -1.969809 \times 10^{-3}$ K^{-1}, $a_2 = 5.030618 \times 10^{-6}$ K^{-2}, $a_3 = -3.878712 \times 10^{-9}$ K^{-3}, $a_4 = 1.058249 \times 10^{-12}$ K^{-4}, R_g =287.0 J/kg K. The specific heat ratio γ is derived from the values of c_p and R_g.

The Reynolds and the Knudsen nondimensional numbers are computed as

$$\mathrm{Re} = \frac{\rho U D_h}{\mu} = \frac{\dot{m} D_h}{\mu A}, \tag{11}$$

and

$$\mathrm{Kn} = \frac{\mathrm{Ma}}{\mathrm{Re}} \sqrt{\frac{\gamma \pi}{2}}, \tag{12}$$

respectively. The former is needed in order to compute the incompressible friction factor depending on the flow regime. The latter is used to check whether the continuum hypothesis, on which the Fanno theory relies, is correct from the physical point of view. In this work the focus is on laminar flows, Re < 2300, and lower Reynolds are always associated to low Mach numbers. From Eq. (12) it is found that in the simulations performed, which are presented below, the Knudsen numbers are always in the range $1.1 \times 10^{-4} \div 1.2 \times 10^{-3}$, making the continuum hypothesis acceptable.

The importance of the local friction factor value for the Fanno flow model accuracy has already been underlined. However, there are other elements that concur to the good predictive capability of the numerical model and deserve attention. These are the local average dynamic pressure and the local bulk temperature. It has already been anticipated how the single average velocity value available from the one-dimensional model at each section is not sufficient to compute these quantities accurately as they ultimately depend on the velocity profile. This is an intrinsic limit of the one-dimensional formulation that yet can be overcome.

In the following, quasi-2D correction terms for the proper assessment of the dynamic pressure and of the temperature mean values in a generic section of the micro-channel are introduced for both the cases of incompressible and compressible flows. These terms are based on the actual velocity profiles encountered in the channel. The impact of compressibility over the friction factor is also investigated. Correlations for the calculation of the three highlighted quantities are given in the end. The correlations are shown to grant a very good match between the predictions of the 1D model and the CFD results compared to the standard Fanno flow-based 1D model.

3.1. Dynamic pressure

Let us consider the p stopping criterion described above. If no outlet extra pressure drops are considered, this is equivalent to state that the total pressure at the channel outlet must equal the downstream stagnation pressure boundary condition imposed

$$p_{out} + p_{d,out} = p_{t,out} = p_1. \tag{13}$$

The inevitable channel exit pressure drop, technically, can be easily modelled by means of a concentrated and/or distributed loss term to be subtracted to $p_{t,out}$ in Eq. (13).

For a proper response of the model, it is important not only to compute p from Eq. (2) or similar, but also to evaluate the dynamic pressure p_d correctly so that the numerical model will stop at the right moment, when Eq. (13) is satisfied.

In the one-dimensional model we obtain single values of density and velocity at each section, and the dynamic pressure can be easily computed as

$$p_d = \frac{\rho U^2}{2}. \tag{14}$$

Yet, this is correct only if the velocity is uniform over the section, which is not the case. Thus, the right-hand term in Eq. (14) needs to be adjusted in order to account for the non-uniform velocity profile. Doing so the average dynamic pressure can be evaluated properly in terms of the available average quantities, which are the sole data the one-dimensional model can provide

$$p_{d,avg} = g \cdot \frac{\rho_{blk} U_{avg}^2}{2}. \tag{15}$$

The term g is of course function of the velocity profile which in turn depends on the Mach number, the flow regime, and the channel cross-section.

In Section 4 a number of correction terms will be given for different channel cross-sections under the assumption of laminar incompressible velocity profile (Poiseuille flow). The terms come from the integration of Eq. (14) over the cross-section and are extended into compressible flow correlations in Section 6.

3.2. Temperature

Substituting Eq. (1) into Eq. (4), it is possible to express the gas flow temperature drop in the channel in function of the Mach number

$$\frac{T_0}{T} = 1 + \frac{\gamma - 1}{2} \mathrm{Ma}^2, \tag{16}$$

or, with a few algebraic steps

$$(T_0 - T) = \frac{U^2}{2 c_p}. \tag{17}$$

This equation basically poses a limit to the fluid cooling at the channel outlet when the flow is choked starting from a subsonic inlet condition. For instance, if the gas is air with a stagnation temperature of 300 K and a heat capacity ratio of 1.4, the outlet fluid temperature will drop at most to 250 K.

Once again, this result is obtained considering a single velocity value over the channel section, coherently with the one-dimensional model limits. Thus, also the right-hand term in Eq. (17) needs to be adjusted to account for the non-uniform velocity profile effect over the bulk temperature

$$(T_0 - T_{blk}) = g \cdot \frac{U_{avg}^2}{2c_{p,blk}}. \tag{18}$$

Here we refer to the mass-weighted average, or bulk, temperature as this is the proper average value to be used in the energy conservation equation.

In the next section a number of g terms will be given for different channel cross-sections under the assumption of Poiseuille flow. The terms come from the integration of Eq. (17) over the cross-section. This will also allow a better prediction of the fluid thermophysical properties overall. It will be shown that the one-dimensional temperature drop limit discussed above will actually be marginally broken ($g > 1$) when the flow is choked, coherently with the CFD results.

4. Laminar incompressible flow terms

Let us start considering the case of incompressible laminar Poiseuille flow. The dynamic pressure and the bulk temperature are computed analytically in function of the average velocity for the cases a of circular section, for the parallel-plates channel, for the generic annular section, and for the generic rectangular cross-section. The Poiseuille number $\mathrm{Po} = f \cdot \mathrm{Re}$ is also computed for each case.

4.1. Circular cross-section channel

According to the Poiseuille theory the velocity profile in a section of a circular cross-section pipe of radius R and radial coordinate r is given by

$$U(r) = \frac{1}{4\mu}\frac{\mathrm{d}p}{\mathrm{d}x}(R^2 - r^2) = U_{max}\left(1 - \frac{r^2}{R^2}\right), \tag{19}$$

while the average velocity can be written, after integration, as

$$U_{avg} = \frac{\int_0^R U(r) r \mathrm{d}r}{\int_0^R r \mathrm{d}r} = \frac{1}{2} \cdot U_{max}. \tag{20}$$

Similarly, the area-weighted average of the dynamic pressure in the section is

$$p_{d,avg} = \frac{\int_0^R \frac{\rho U(r)^2}{2} r \mathrm{d}r}{\int_0^R r \mathrm{d}r} = \frac{4}{3} \cdot \frac{\rho_{blk} U_{avg}^2}{2}. \tag{21}$$

Thus, considering the laminar incompressible velocity profile in a circular cross-section channel, Eq. (21) should be used in place of Eq. (14) for computing the average dynamic pressure correctly.

It will be shown that as the compressibility effects become important, the velocity profile will tend to flatten, gradually shifting the 4/3 coefficient towards 1 according to rules to be determined. The same consideration applies to the other quantities and to the other cross-section types considered in the following.

The bulk temperature is derived from

$$T_{blk} = \frac{\int_0^R \rho U(r)\left(T_0 - \frac{U(r)^2}{2c_p}\right) r \mathrm{d}r}{\int_0^R \rho U(r) r \mathrm{d}r} = T_0 - 2 \cdot \frac{U_{avg}^2}{2c_{p,blk}}. \tag{22}$$

From the definition of friction factor in the channel

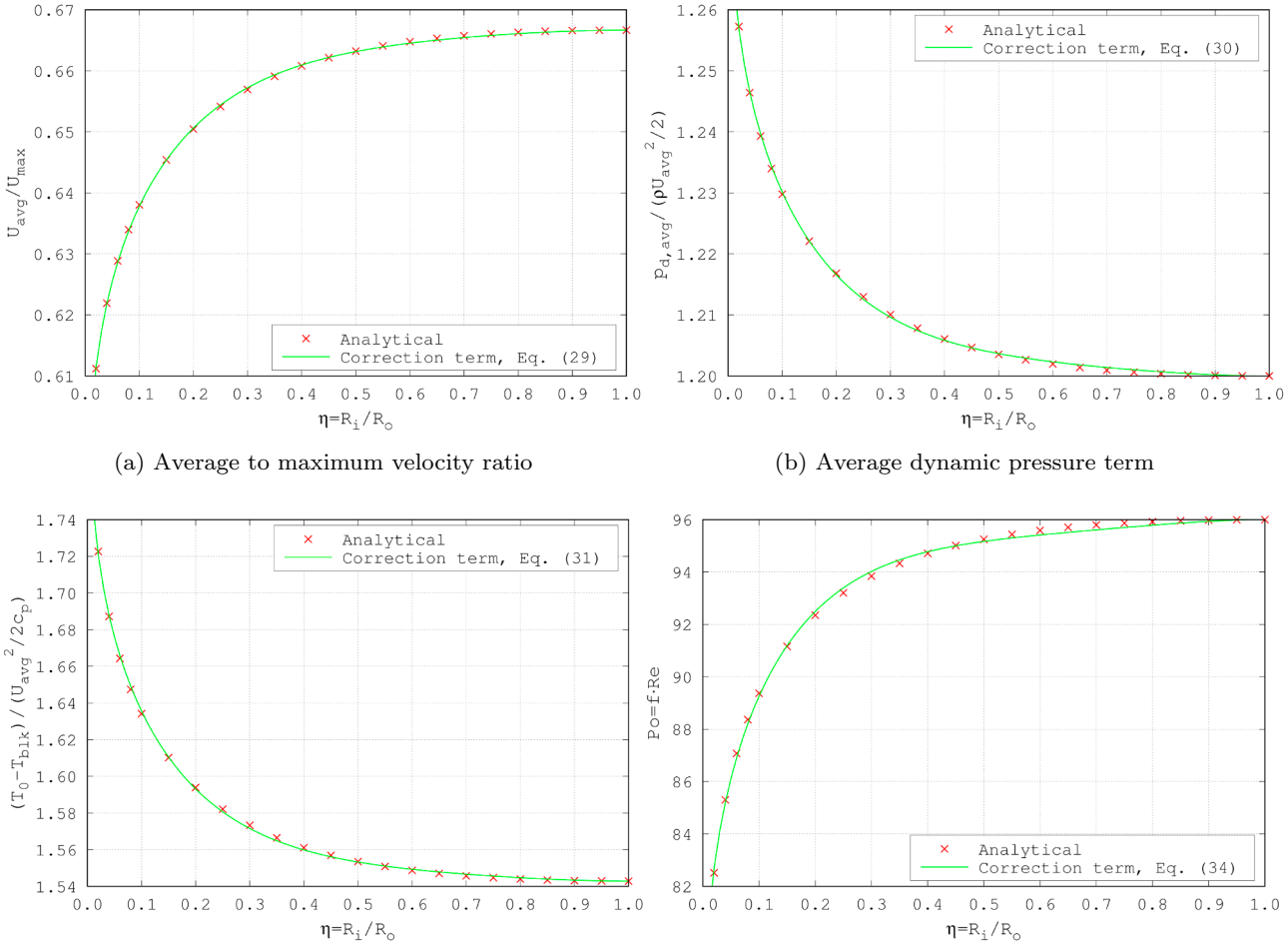

(a) Average to maximum velocity ratio

(b) Average dynamic pressure term

(c) Bulk temperature term

(d) Poiseuille number

Fig. 1. Annular channel analytical correction terms and their approximation functions.

$$f = \frac{8\ |\tau_w|}{\rho_{blk} U_{avg}^2}, \tag{23}$$

considering that

$$|\tau_w| = \mu_{blk} \left|\frac{\partial U}{\partial r}\right|_{r=R} = \frac{4\mu_{blk} U_{avg}}{R}, \tag{24}$$

with a few algebraic steps the well-known formula

$$f = \frac{64}{\mathrm{Re}} \tag{25}$$

is found.

4.2. Parallel-plates channel

For a parallel-plates channel of height H

$$U(y) = \frac{1}{2\mu}\frac{\mathrm{d}p}{\mathrm{d}x}\frac{y}{H}\left(1 - \frac{y}{H}\right) = 4U_{max}\frac{y}{H}\left(1 - \frac{y}{H}\right), \tag{26}$$

where y is the heightwise coordinate. The average velocity is

$$U_{avg} = \frac{\int_0^H U(y)\mathrm{d}y}{\int_0^H \mathrm{d}y} = \frac{2}{3}\cdot U_{max}, \tag{27}$$

while for the area-weighted average of the dynamic pressure we have

$$p_{d,avg} = \frac{\int_0^H \frac{\rho U(y)^2}{2}\mathrm{d}y}{\int_0^H \mathrm{d}y} = \frac{6}{5}\cdot\frac{\rho_{blk} U_{avg}^2}{2}. \tag{28}$$

The bulk temperature is

$$T_{blk} = \frac{\int_0^H \rho U(y)\left(T_0 - \frac{U(y)^2}{2c_p}\right)\mathrm{d}y}{\int_0^H \rho U(y)\mathrm{d}y} = T_0 - \frac{54}{35}\cdot\frac{U_{avg}^2}{2c_{p,blk}}. \tag{29}$$

In this case the wall shear stress is

$$|\tau_w| = \mu_{blk}\left|\frac{\partial U}{\partial y}\right|_{y=0\ y=H} = \frac{6\mu_{blk} U_{avg}}{H}, \tag{30}$$

from which

$$f = \frac{96}{\mathrm{Re}} \tag{31}$$

follows.

4.3. Annular channel

For an annular cross-section channel of inner radius R_i and outer radius R_o the velocity profile is

$$U(r) = \frac{1}{4\mu}\frac{\mathrm{d}p}{\mathrm{d}x}\left[(R_i^2 - r^2) + (R_o^2 - R_i^2)\frac{\ln(r/R_i)}{\ln(R_o/R_i)}\right]. \tag{32}$$

By differentiating Eq. (32), the radial coordinate at which the velocity is maximum can be computed as

$$r_{U_{max}} = \sqrt{\frac{1}{2}\frac{R_o^2 - R_i^2}{\ln(R_o/R_i)}}, \tag{33}$$

and falls a bit closer to the inner wall than to the outer, the gap being inversely proportional to the radii ratio $\eta = R_i/R_o$.

In this case all the correction terms are found to depend on η as in Fig. 1. To be noted that for $\eta \to 1$ the quantities U_{avg}, $p_{d,avg}$, T_{blk}, and f tend to the parallel-plates value, while for $\eta \to 0$ they tend to the circular channel value. These limits are approached with null derivative at $\eta \to 1$ and infinite derivative at $\eta \to 0$. Thus, the lines in Fig. 1 cannot be well interpolated by low-order polynomials, better approximating functions are deemed to be the following

$$U_{avg} = \frac{\int_{R_i}^{R_o} U(r)r\mathrm{d}r}{\int_{R_i}^{R_o} r\mathrm{d}r} = \left[\frac{1}{2} + \left(\frac{2}{3} - \frac{1}{2}\right)\eta^{0.1086 - 0.2956\eta + 0.3730\eta^2 - 0.1860\eta^3}\right]\cdot U_{max}, \tag{34}$$

$$p_{d,avg} = \frac{\int_{R_i}^{R_o} \frac{\rho U(r)^2}{2} r\mathrm{d}r}{\int_{R_i}^{R_o} r\mathrm{d}r} = \left[\frac{4}{3} + \left(\frac{6}{5} - \frac{4}{3}\right)\eta^{0.1508 - 0.4550\eta + 0.6313\eta^2 - 0.3271\eta^3}\right]\cdot\frac{\rho_{blk} U_{avg}^2}{2}, \tag{35}$$

$$T_{blk} = \frac{\int_{R_i}^{R_o} \rho U(r)\left(T_0 - \frac{U(r)^2}{2c_p}\right)r\mathrm{d}r}{\int_{R_i}^{R_o} \rho U(r) r\mathrm{d}r} = T_0 - \left[2 + \left(\frac{54}{35} - 2\right)\eta^{0.1340 - 0.4065\eta + 0.5475\eta^2 - 0.2750\eta^3}\right]\cdot\frac{U_{avg}^2}{2c_{p,blk}}. \tag{36}$$

For the annular cross-section channel, the wall shear stress is different for the inner and for the outer wall

$$|\tau_w| = \mu_{blk}\left|\frac{\partial U}{\partial r}\right|_{r=R_i r=R_o} = \begin{cases} \frac{1}{4}\frac{\mathrm{d}p}{\mathrm{d}x}\left(\frac{1}{R_i}\frac{R_o^2 - R_i^2}{\ln(R_o/R_i)} - 2R_i\right) & \text{for } r = R_i \\ \frac{1}{4}\frac{\mathrm{d}p}{\mathrm{d}x}\left(\frac{1}{R_o}\frac{R_o^2 - R_i^2}{\ln(R_o/R_i)} - 2R_o\right) & \text{for } r = R_o \end{cases}. \tag{37}$$

Thus, the area-weighted average of the wall shear stress should rather be computed

$$|\tau_{w,avg}| = \frac{1}{2}\frac{\mathrm{d}p}{\mathrm{d}x}\left(\frac{R_o - R_i}{\ln\left(\frac{R_o}{R_i}\right)} - \frac{R_o^2 + R_i^2}{R_o + R_i}\right), \tag{38}$$

and used to approximate the friction factor as follows

$$f = \left[\frac{2}{3} + \left(1 - \frac{2}{3}\right)\eta^{0.1479 - 0.5335\eta + 0.8688\eta^2 - 0.4832\eta^3}\right]\cdot\frac{96}{\mathrm{Re}}. \tag{39}$$

All the approximations given here result in a maximum interpolation error < 0.2% compared to the analytical solution.

4.4. Rectangular channel

Let us consider a rectangular channel of height H and width W. From the theory [33], the velocity profile is given by the series

$$U(y,z) = \frac{H^2}{2\mu}\frac{\mathrm{d}p}{\mathrm{d}x}\frac{y}{H}\left(1 - \frac{y}{H}\right) - \frac{4H^2}{\mu\pi^3}\frac{\mathrm{d}p}{\mathrm{d}x}\sum_{n=1}^{\infty}\frac{1}{\delta_n^3}\frac{\sinh\left(\delta_n\pi\frac{z}{H}\right) + \sinh\left(\delta_n\pi\frac{W-z}{H}\right)}{\sinh\left(\delta_n\pi\frac{W}{H}\right)}\sin\left(\delta_n\pi\frac{y}{H}\right), \tag{40}$$

where $\delta_n = (2n - 1)$, $0 \leqslant y \leqslant H$, $0 \leqslant z \leqslant W$. In Eq. (40) there is no requirement on which is the major dimension so that H and y could be swapped with W and z without affecting the results. We assume the cross-section aspect ratio $\beta \leqslant 1$, that is to say $\beta = \min(W/H,\ H/W)$. Also in this case the correction terms are not constant and depend on β. The quantities U_{avg}, $p_{d,avg}$, T_{blk}, and f tend to the parallel-plates value as $\beta \to 0$, and have zero gradient for $\beta = 1$.

The series in Eq. (40) can be integrated with an algebraic manipulator even though, due to its complexity, any PC will run out of memory soon if n is kept large. Luckily the terms of the series tend quickly to zero so that the computational resources are not a real issue for an accurate solution.

The open source Maxima package, available from the internet, is used for computing the integrals up to the degree that is possible to handle with an ordinary workstation having 12 GB of ram. The results are reported in Fig. 2 and are well approximated by the following polynomial functions

$$U_{avg} = \frac{\int_0^W \int_0^H U(y,z)\mathrm{d}y\mathrm{d}z}{\int_0^W \int_0^H \mathrm{d}y\mathrm{d}z} = \frac{2}{3}\left[1 - 0.5992\beta - 0.6105\beta^2 + 2.8221\beta^3 - 2.8424\beta^4 + 0.9447\beta^5\right]\cdot U_{max} \tag{41}$$

computed up to $n = 14$ (see Fig. 2a),

$$p_{d,avg} = \frac{\int_0^W \int_0^H \frac{\rho U(y,z)^2}{2} \mathrm{dydz}}{\int_0^W \int_0^H \mathrm{dydz}} = \frac{6}{5}[1 + 0.3200\beta - 0.0582\beta^2 - 0.2524\beta^3 + 0.1384\beta^4] \cdot \frac{\rho_{blk} U_{avg}^2}{2} \tag{42}$$

computed up to $n = 8$ (see Fig. 2b),

$$T_{blk} = \frac{\int_0^W \int_0^H \rho U(y,z) \left(T_0 - \frac{U(y,z)^2}{2c_p}\right) \mathrm{dydz}}{\int_0^W \int_0^H \rho U(y,z) \mathrm{dydz}} = T_0 - \frac{54}{35}[1 + 0.6113\beta + 1.2052\beta^2 - 3.6217\beta^3 + 3.1671\beta^4 - 0.9650\beta^5] \cdot \frac{U_{avg}^2}{2c_{p,blk}} \tag{43}$$

computed up to $n = 6$ (see Fig. 2c). The wall shear stress changes with continuity along the rectangular perimeter. We thus compute the average wall shear stress as the area-weighted average of the average stress along H and the one along W

$$|\tau_{w,avg}| = \frac{|\tau_{w,avg,y}| \, W + |\tau_{w,avg,z}| \, H}{W + H} = \frac{\left| \int_0^W \mu \left(\frac{\partial U}{\partial y}\right)_{y=0 \, y=H} \mathrm{dz} \right| + \left| \int_0^H \mu \left(\frac{\partial U}{\partial z}\right)_{z=0 \, z=W} \mathrm{dy} \right|}{W + H}. \tag{44}$$

From this, the friction factor can be approximated by

$$f = [1 - 1.3652\beta + 2.0024\beta^2 - 1.8095\beta^3 + 1.0381\beta^4 - 0.2727\beta^5] \cdot \frac{96}{\mathrm{Re}} \tag{45}$$

computed up to $n = 14$ (see Fig. 2d). This formula is equivalent to the well-known one proposed by Shah and London in [26], given below as Eq. (46).

$$f = [1 - 1.3553\beta + 1.9467\beta^2 - 1.7012\beta^3 + 0.9564\beta^4 - 0.2537\beta^5] \cdot \frac{96}{\mathrm{Re}}. \tag{46}$$

Compared to that, the different coefficients give a slightly lower interpolation error and a null derivative at $\beta = 1$. All the approximations given here result in a maximum interpolation error < 0.1% compared to the analytical solution.

Table 2 resumes the correction terms found in the present section. It is reminded that these coefficients hold for the case of incompressible laminar flow and that, with the exclusion of the last row, all the coefficients will progressively shift towards 1 when the velocity profile becomes flatter, that is to say when the flow becomes turbulent or when the Mach number approaches unity, as will be explained in the following section.

5. Compressible velocity profiles

In order to better understand the effects of compressibility on the flow, the evolution of the velocity profiles in the channel is now analysed. For this purpose, a set of 40 CFD simulations is solved.

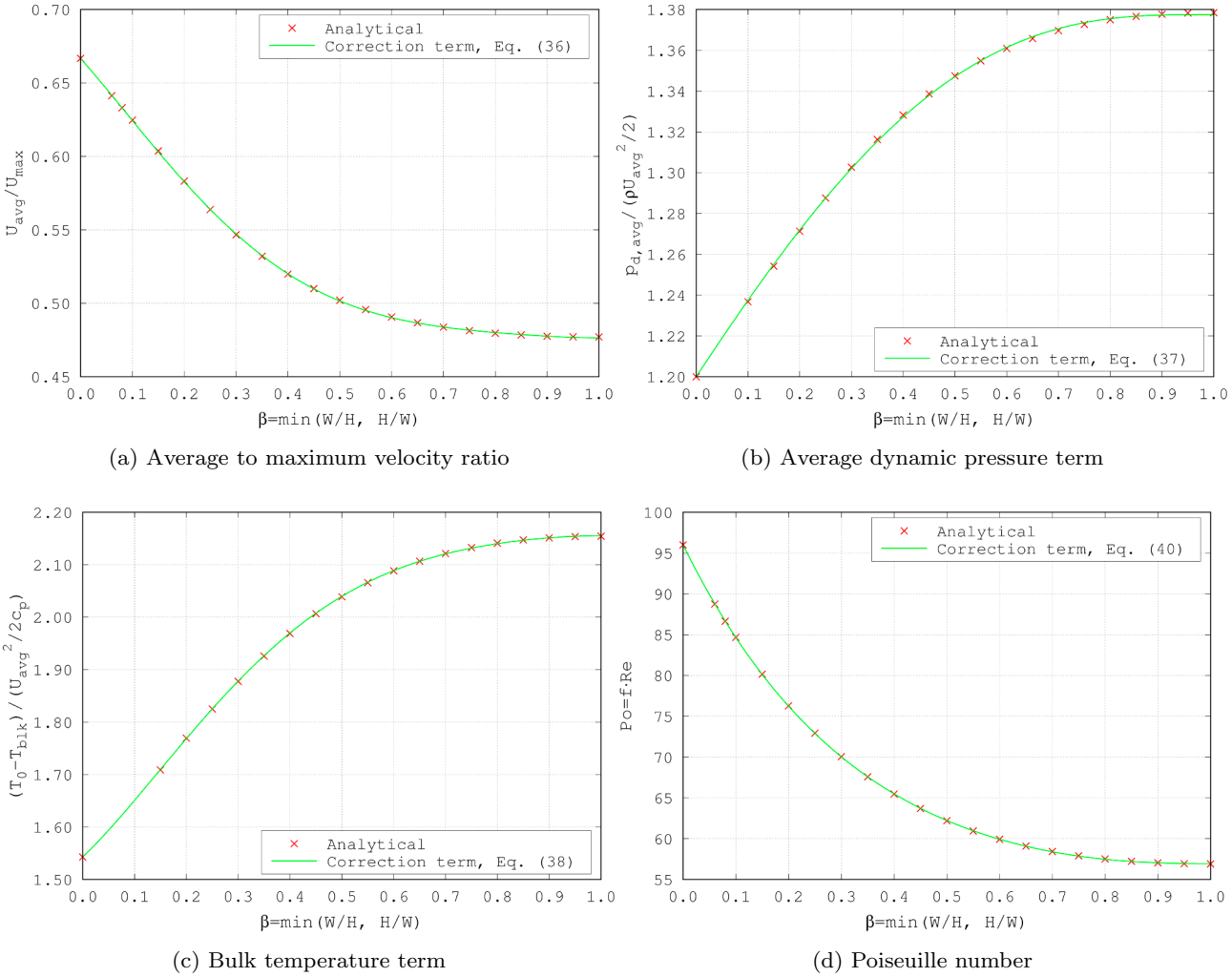

(a) Average to maximum velocity ratio

(b) Average dynamic pressure term

(c) Bulk temperature term

(d) Poiseuille number

Fig. 2. Rectangular channel analytical correction terms and their approximation functions.

Table 2
Correction terms synoptic table for the incompressible laminar flow.

Quantity	Circular	Parallel-Plates	Annular Channel			Rectangular Channel		
	Channel	Channel	$\eta \to 1$	$\eta = 2$	$\eta \to \infty$	$\beta \to 0$	$\beta = 0.5$	$\beta = 1$
U_{avg}/U_{max}	1/2	2/3	2/3	0.6632	1/2	2/3	0.5021	0.4770
$P_{d,avg}/(\rho_{blk} U_{avg}^2/2)$	4/3	6/5	6/5	1.2035	4/3	6/5	1.3475	1.3784
$(T_0 - T_{blk})/(U_{avg}^2/2c_{p,blk})$	2	54/35	54/35	1.5535	2	54/35	2.0388	2.1542
$\mathrm{Po} = f \cdot \mathrm{Re}$	64	96	96	95.250	64	96	62.192	56.908

5.1. Simulations setup

The simulations were chosen in order to span the Mach numbers in the subsonic region ($0 \leqslant \mathrm{Ma} \leqslant 1$), and the Reynolds numbers in the laminar region ($0 \leqslant \mathrm{Re} \leqslant 2300$). Two channel cross-section types were investigated (circular and parallel-plates), for two aspect ratios ($\alpha = 100$ and $\alpha = 500$), and two stagnation temperatures ($T_0 = 300$ K and $T_0 = 500$ K). For each permutation of these 3 parameters 5 simulations were performed with growing upstream stagnation pressure, while the downstream stagnation pressure was kept at 1 bar. The rationale was to span the largest possible range of Mach numbers up to meeting the sonic condition at the channel outlet for the largest pressure in the set. The hydraulic diameter of the channel was set to $D_h = 100\ \mu$m: for the given conditions, this choice allowed a wide range of Reynolds numbers to be investigated, while still remaining in the laminar region. Annular and rectangular cross-sections from now on are dropped.

The simulations were solved with the Ansys Fluent code. The mesh was either axisymmetric (for the circular cross-section cases) or planar (for the parallel-plates cross-section cases), and fully structured with the maximum values of y^+ always below 0.3. Plenums were created at the channel ends by gradually expanding the cross-section up to when its area becomes 300 times that of the channel. In this way, pressure boundary conditions were set at locations where the static and the total pressure almost coincide. Depending on the cases, the mesh size ranges between 150 thousand and 1.5 million elements. An off-scale 1000 elements mesh example is shown in Fig. 3. Second-order discretization schemes and a coupled solver were chosen. Even though the flow is expected to be laminar, an SST k-ω turbulence model was adopted, resulting in extremely low values of the turbulent quantities throughout the domain as expected. During the early testing stage of the numerical model this was seen to ensure a faster and more stable convergence, in particular during the first iterations when the flow field still has to settle into a stable solution. Overall, the set of equations solved was the following

$$\begin{cases} \nabla\cdot(\rho\mathbf{U}) = 0 & \text{Mass conservation} \\ \nabla\cdot(\rho\mathbf{U}\mathbf{U}) = -\nabla p + \nabla\cdot\tau & \text{Momentum conservation} \\ \nabla\cdot(\rho\mathbf{U}(E + p/\rho)) = \nabla\cdot(\lambda_{eff}\nabla T + \tau\cdot\mathbf{U}) & \text{Energy conservation} \\ \nabla\cdot(\rho\mathbf{U}k) = \nabla\cdot(\Gamma_k\nabla k) + G_k - Y_k & \text{Transport of } k \\ \nabla\cdot(\rho\mathbf{U}\omega) = \nabla\cdot(\Gamma_\omega\nabla\omega) + G_\omega - Y_\omega + Z_\omega & \text{Transport of } \omega \end{cases} \tag{47}$$

where τ is the stress tensor, E the total energy, $\tau\cdot\mathbf{U}$ the viscous heating term, k the turbulence kinetic energy, and ω the specific dissipation rate. In the last two transport equations Γ represents the effective diffusivity, G the production, Y the dissipation, and Z the cross-diffusion terms. With reference to Fig. 3, the boundary conditions are as follows: total pressure and temperature imposed at the inlet (boundary on the left), static pressure equal to 1 bar imposed at the outlet (boundary on the right), no-slip condition at the walls (upper boundary), and, depending on the cross-section type, either axial symmetry or symmetry plane on the bottom boundary.

The results of the mesh convergence study is shown in Fig. 4. The image shows the friction factor predicted by the CFD at two locations along the channel (one half way, the other close to the outlet section) for two test cases (one where the Mach number at the outlet is low, the other where $\mathrm{Ma}_{out} = 1$). As different velocity gradients require different mesh resolution to be caught accurately, the mesh was adaptively chosen to always grant a maximum $y^+ < 0.3$. In this way low Mach cases will have a thicker mesh, and high Mach cases a finer mesh. In Fig. 4 the friction factor is plotted against the local y^+, and also the number of elements of the tested meshes is reported. According to the asymptotic value that can be evinced from the data, the mesh chosen is able to grant a maximum error in the prediction of the friction factor < 0.2% under any circumstance. Similar conclusions have been drawn for other quantities of interest and other test cases, and are omitted for brevity.

All the simulations were run up to a convergence level with the maximum residual $<10^{-7}$. Out of 40 simulations 37 reached this level of convergence. The remaining 3 showed an unexpected and erroneous transition to turbulence, accompanied with the inability to reach a stable solution and a good level of convergence, and were thus discarded.

During the post-processing, the velocity profiles in the channels were extracted every 5 D_h for the cases with $\alpha = 100$, and every 10 D_h for the cases with $\alpha = 500$. A finer step was adopted close to the channel ends. Additional samples were also taken close to the channel outlet for the choked flow cases. This was needed in order to populate the region where $0.8 \leqslant \mathrm{Ma} \leqslant 1.0$ which otherwise would have been under-sampled. 1638 velocity profiles have been extracted overall. At the same locations, information on the static and the total pressure, the temperature, the velocity, the Mach number, the wall shear stress, and the thermodynamic properties of the fluid was registered as well.

5.2. Velocity profiles evolution

Fig. 5 shows the evolution of the velocity profiles for a choked flow case. In Fig. 5a it is shown how the axial velocity profile is rather flat at the channel inlet due to the fact that the flow is far from being developed. Then, the entrance effects diminish quickly and the velocity profile becomes quasi-parabolic, remaining almost the same for a large portion of the channel. In this region we can say that the flow is close to the fully-developed condition, even though the concept of fully-

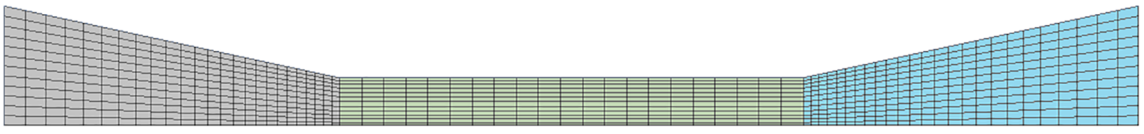

Fig. 3. Off-scale mesh example, from [15].

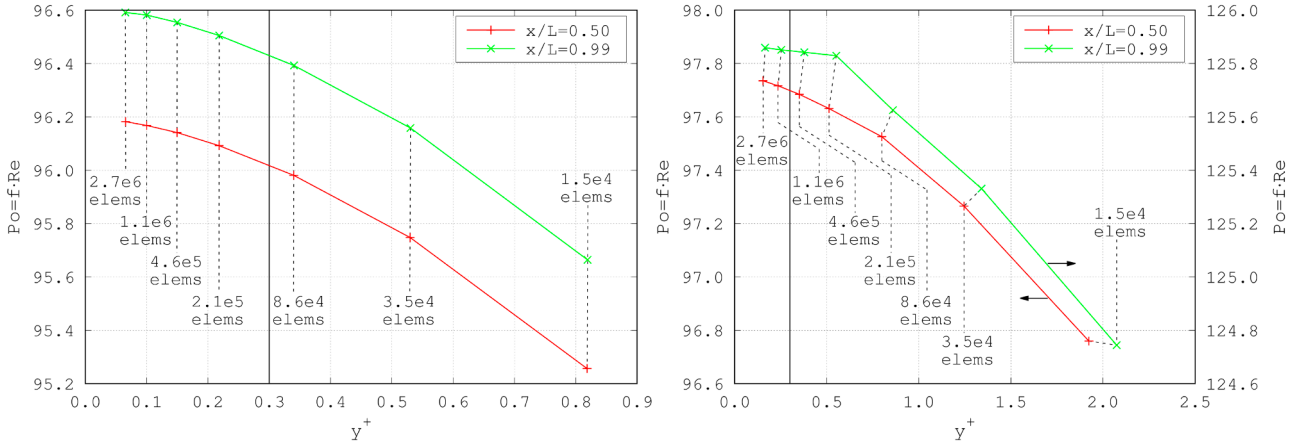

(a) Low Mach case

(b) High Mach case: the arrows indicate the reference abscissae axis for each line.

Fig. 4. CFD mesh convergence study: the vertical line indicates the y^+ constraint the mesh must satisfy in order to be accepted.

developed flow, strictly speaking, is only applicable to incompressible flows. We call this profile quasi-parabolic since the Mach number, in this case, is slightly above 0.3 and the compressibility effects, even if marginal, are not fully negligible so that the flow cannot be assimilated to a Poiseuille flow. Close to the channel outlet, as the Mach number grows, the compressibility effects become more important and the profiles tend to flatten again.

If the axial velocity profile changes in shape, it means that mass is

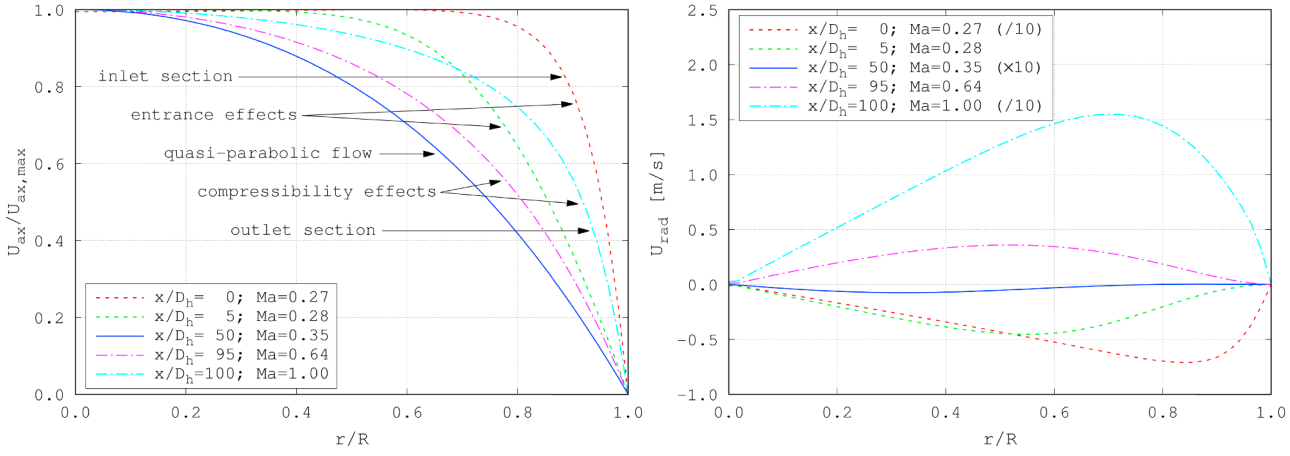

(a) Normalized axial velocity profiles

(b) Radial velocity profiles

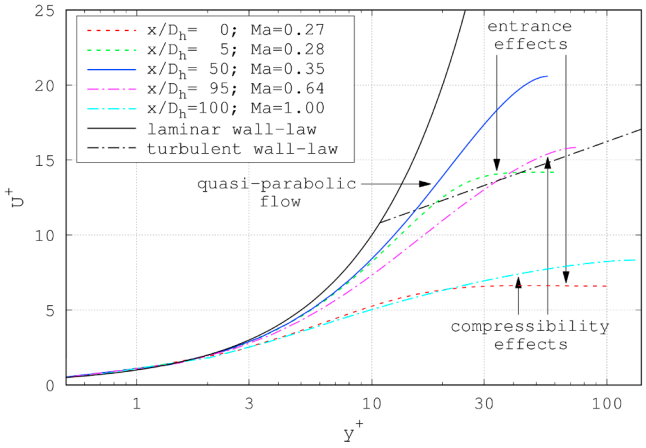

(c) Axial velocity profiles on the y^+ vs U^+ plane

Fig. 5. Velocity profiles evolution from the inlet to the outlet section. The figure refers to the circular cross-section, $\alpha = 100$, $T_0 = 500$ K, $p_0 = 4$ bar case. In this configuration the flow is choked, thus Ma = 1 at the channel outlet.

transferred radially (or transversely, if we consider the parallel-plates cross-section) to make this change possible. The radial velocity profiles are reported in Fig. 5b. Clearly, the radial velocity is almost null in the quasi-parabolic region remaining well below 0.01 m/s, while it grows very quickly close to the channel ends becoming larger than 15 m/s at some point. When the entrance effects dominate, the radial velocity is negative, meaning that mass is transferred towards the centre of the channel so that the flat velocity profiles becomes quasi-parabolic. On the contrary, when the compressibility effects dominate, the radial velocity is positive, meaning that the mass is radially transferred towards the wall, making the velocity profile flatter.

Fig. 5b shows the axial velocity profiles again, but plotted on the nondimensional y^+ vs U^+ plane. Let us consider the quasi-parabolic flow line. The line follows the laminar law of the wall closely for low values of y^+ then gradually departs from it. This is due to the fact that the flow is confined and the pipe centre is already reached for $y^+ \approx 50$. Close to the channel ends, the entrance and the compressibility effects also intervene by further pushing the profiles down as if the flow was turbulent.

In order to quantify the impact of the confined flow on the laminar law of the wall let us compute the values of the wall coordinate y^+ and of the dimensionless velocity U^+ on the axis of a circular cross-section pipe crossed by an incompressible laminar flow. The wall coordinate is defined as

$$y^+ = \frac{(R-r)U_\tau}{\nu}, \tag{48}$$

where $(R-r)$ is the distance from the wall. The dimensionless velocity is

$$U^+ = \frac{U}{U_\tau}, \tag{49}$$

where the friction velocity is

$$U_\tau = \sqrt{\frac{\tau_w}{\rho_{blk}}}. \tag{50}$$

The law of the wall states that, for a laminar flow, close to the wall the equation

$$U^+ = y^+ \tag{51}$$

holds. In case of turbulent flow, instead, the linear law of Eq. (51) holds for $y^+ \leqslant 5$, and is substituted by the log-law

$$U^+ = \frac{1}{\kappa}\ln y^+ + C^+, \tag{52}$$

where $\kappa = 0.41$ and $C^+ = 5.0$, for $y^+ > 30$. The region in between is called buffer layer and is not suitably approximated by either law.

On the pipe axis $r = 0$ and $U = U_{max}$, by recalling Eqs. (20) and (24), and with a few algebraic steps, equations

$$y_c^+ = 2\sqrt{\frac{U_{avg}\rho_{blk}R}{\mu_{blk}}} = 2\sqrt{\frac{\dot{m}}{\mu_{blk}\pi R}}, \tag{53}$$

and

$$U_c^+ = \sqrt{\frac{U_{avg}\rho_{blk}R}{\mu_{blk}}} = \sqrt{\frac{\dot{m}}{\mu_{blk}\pi R}} = \frac{y_c^+}{2}, \tag{54}$$

are found. Similarly for the parallel-plates cross-section channel, we have at the centre of the channel

$$y_c^+ = \sqrt{\frac{3}{2}\cdot\frac{U_{avg}\rho_{blk}H}{\mu_{blk}}} = \sqrt{\frac{3}{2}\cdot\frac{\dot{m}}{\mu_{blk}W}}, \tag{55}$$

where $\dot{m}/W$ is the mass flow rate per unit width, and

$$U_c^+ = \frac{1}{2}\sqrt{\frac{3}{2}\cdot\frac{U_{avg}\rho_{blk}H}{\mu_{blk}}} = \frac{1}{2}\sqrt{\frac{3}{2}\cdot\frac{\dot{m}}{\mu_{blk}W}}, \tag{56}$$

still yielding

$$U_c^+ = \frac{y_c^+}{2}. \tag{57}$$

Thus, the velocity profiles plotted on the nondimensional plane start at $U^+ = y^+$ and terminate at $U^+ = y^+/2$ if the flow is incompressible, while they terminate at $U^+ < y^+/2$ if the flow is compressible or non-developed. The maximum value of y^+ is reached at the channel centre and, for a given geometry, primarily depends on the mass flow rate crossing the channel.

More in general, from simple algebraic considerations, the incompressible velocity profile on the nondimensional plane follows a parametric curve of the type

$$\begin{cases} y^+ = 2C\cdot(1-t) \\ U^+ = C\cdot(1-t^2) \end{cases} \quad \text{for} 0 \leqslant t \leqslant 1, \tag{58}$$

where C is a constant. The same result is valid for both the circular and the parallel-plates cross-sections.

5.3. Velocity profiles and compressibility effects

In order to analyse the impact of compressibility on the velocity profiles we now want to compare all the profiles extracted from the simulations. Of course the set of the 1638 profiles collected must be cleared from any unsuitable sample. After removing the profiles where

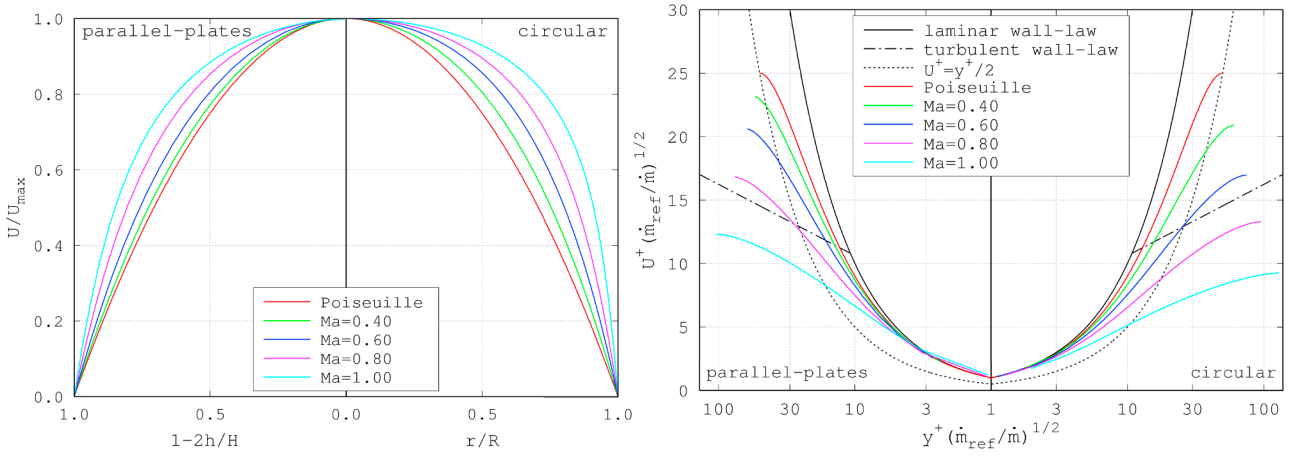

(a) Normalized axial velocity profiles

(b) Axial velocity profiles on the y^+ vs U^+ plane

Fig. 6. Velocity profiles for different Mach numbers: parallel-plates vs circular cross-section channels.

the entrance effects are evident and those belonging to the non-converged simulations, 700 profiles are left: 408 relative to the circular cross-section, and 292 relative to the parallel-plates cross-section. By normalizing and plotting these profiles against each other it is evident how those having the same Mach number and the same cross-section type are perfectly superimposable. Besides, no other compressibility-related quantity such as, for instance, the Mach number derivative or the friction factor, is able to return such a perfect match among the profiles. This suggests that the velocity profile in a compressible channel flow of given channel geometry ultimately depends on the Mach number alone. This result was expected and was already found in [13] and in [14]. The governing equations, in fact, ultimately depend on the Mach number and, through the friction factor, on the Reynolds number alone. Yet, it is well known that in laminar internal flows the velocity profile is not affected by the Reynolds number, and regarding this compressible flows make no exception.

As already discussed in Section 5.2, the profiles shift from parabolic becoming flatter as the Mach number grows. Fig. 6 shows the normalized velocity profiles obtained for different Mach numbers for both the circular and the parallel-plates cross-section cases. In Fig. 6a it is evident how the circular cross-section channel undergoes larger profile changes with the Mach number. As the profile becomes flatter, necessarily also the velocity gradient at the wall gets larger, and this affects the friction factor significantly. In Fig. 6b the same profiles are plotted on the nondimensional y^+ vs U^+ plane. As already mentioned, the extent of the lines on this plane depends on the mass flow rate crossing the channel. As the plotted profiles are samples from different simulations, in order to compare them more suitably, the data have been normalized over a reference mass flow rate chosen so that the incompressible profile will reach $y^+ = 2U^+ = 50$ at the channel axis. From there, as the Mach number grows, the profiles drop to lower U^+ and larger y^+ values, and when the flow is choked $U^+ \approx y^+/14$ is attained on the channel axis for the circular cross-section case. Similarly, for the parallel-plates cross-section we find $U^+ \approx y^+/8.4$, in line with the fact that the profile change is less pronounced in this case.

From the analysis of Fig. 5c it can be noted that the locus of points given by the (y^+, U^+) values at the axis lies on a line having equation

$$U^+ = y^+_{inc}\left(\frac{1}{2} - 0.34\ln y^+\right). \tag{59}$$

This formula holds for both the circular and the parallel-plates cross-section cases.

6. Laminar compressible flow correlations

It has been shown how the velocity profiles change with the Mach number. If this happens, then the g coefficients discussed in Section 4 are no longer applicable to compressible flows. We now want to find proper $g(\mathrm{Ma})$ correlations extending the accuracy of the one-dimensional model also for compressible flows in the cases of circular and parallel-plates cross-section channels. These correlation can be easily derived from the results of the CFD simulations. The dynamic pressure

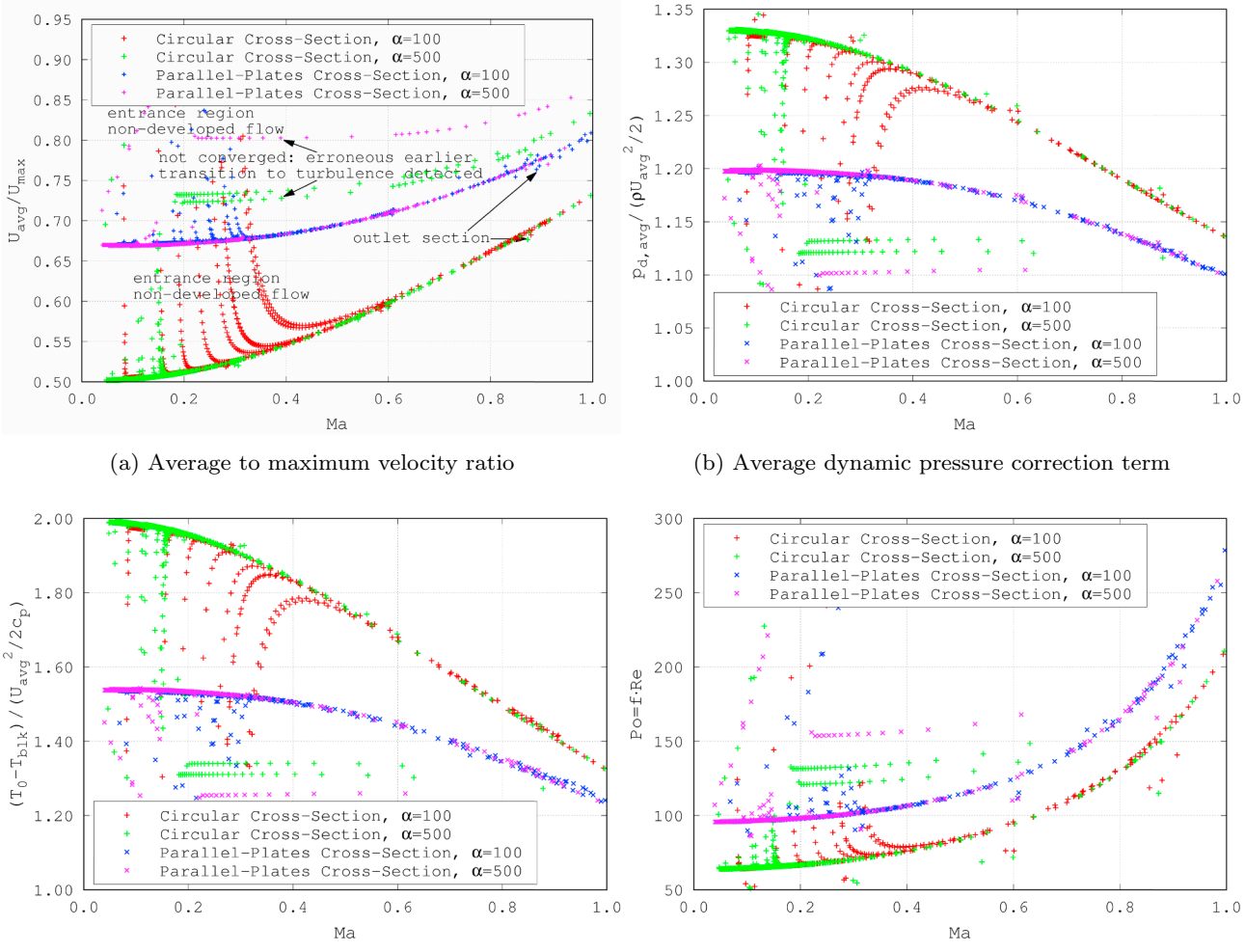

(a) Average to maximum velocity ratio

(b) Average dynamic pressure correction term

(c) Bulk temperature correction term

(d) Poiseuille number

Fig. 7. Compressible correction terms in function of the Mach number from the full set of CFD samples.

and the temperature coefficients at each section can be computed by solving Eqs. (15) and (18) for g since all the other terms are known from the simulations. Similarly for the Poiseuille number, from the definitions of f and Re we have

$$\mathrm{Po} = f \cdot \mathrm{Re} = \frac{8\tau_w D_h}{\mu_{blk} U_{avg}}, \tag{60}$$

where the terms on the right-hand side are known from the simulations. Fig. 7 is the result of plotting the coefficients computed for the 1638 sampled sections versus the Mach number.

Even though the data spread is quite large, two main trend lines are clearly marked in each plot: one relative to the circular cross-section channel, the other to the parallel-plates cross-section channel. Looking more carefully at the data it can be seen that three causes can make the samples deviate from these lines. These are:

- Entrance effects
  The more the velocity profile is non-developed the more the U_{avg}/U_{max} ratio is large because of the flatter profile. This ratio then drops as the profile develops. In Fig. 7a the samples affected by the entrance effects lay in quasi-vertical lines which then gradually link up to the main trend lines. Similar considerations can be derived for each other plot in the figure.
- Non-converged simulations
  The three simulations that, as already reminded, encountered convergence problems were also characterized by an erroneous earlier transition to turbulence. The samples relative to these simulations lay in quasi-horizontal lines in the plots, as highlighted in Fig. 7a. This suggests that the shape of the compressible turbulent velocity profile might be little affected by the Mach number, as long as these simulations can be trusted.
- Outlet section
  If we remove the two previous set of samples, there are still some samples that fall slightly off the main lines, mostly on the opposite side with respect to where the previous sets laid. These correspond to the samples located at channel outlet section or very close to it. There the flow is already affected, to some extent, by the fact that the cross-section begins to expand so that the velocity profile becomes slightly asymmetric in order to follow the expansion.

The set of samples due to the last two causes are easy to be spotted and removed from the global set. The situation is more tricky with the first set since these samples gradually merge with the main lines as the entrance effects are damped, and it is difficult to discriminate clearly between non-developed and developed flow samples. Considering that these samples all lay on the same side of the trend lines it has been chosen to remove them following the idea of Pareto set [34], commonly used in optimization problems to discriminate between optimal and sub-optimal solutions.

Consider Fig. 7a as being the representation of the samples in the space of the solutions of a two-objectives optimization problem whose objectives are the maximization of Ma and the minimization of

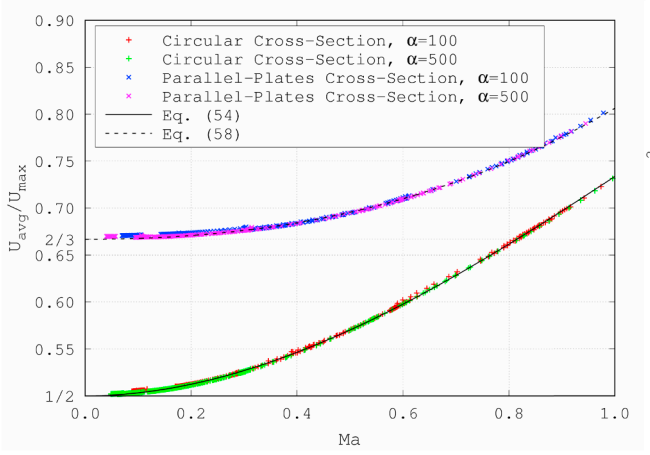

(a) Average to maximum velocity ratio

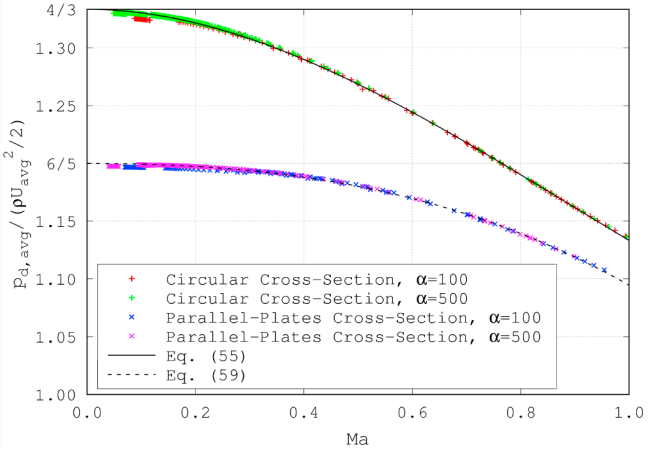

(b) Average dynamic pressure correction term

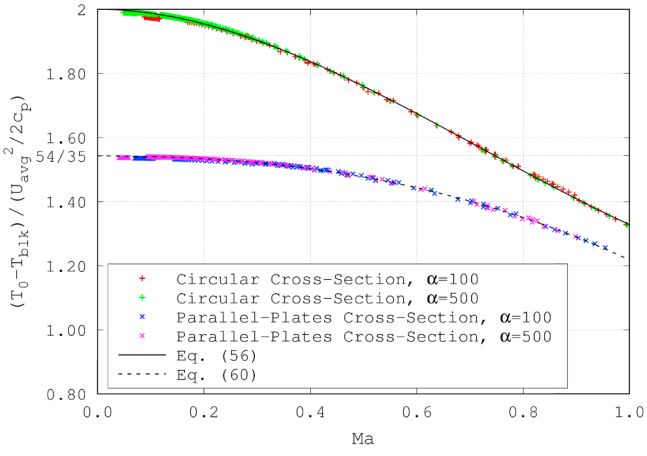

(c) Bulk temperature correction term

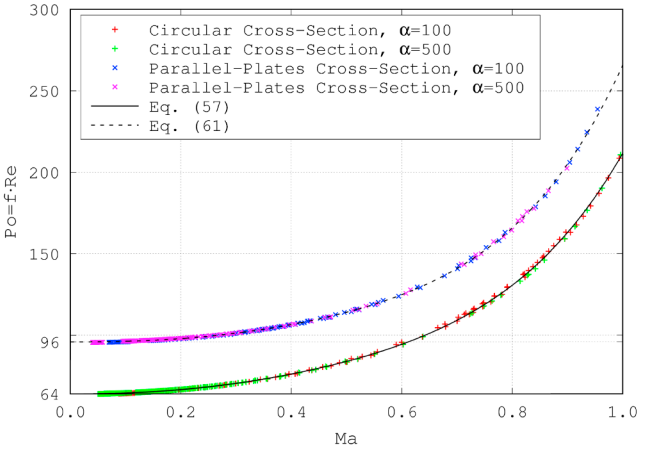

(d) Poiseuille number

Fig. 8. Compressible correction terms in function of the Mach number from the Pareto set of CFD samples.

U_{avg}/U_{max}. Following the logic of Pareto, a sample is optimal and belongs to the Pareto front [35,36], if it is non-dominated, *i.e.* if in the whole set no other sample exists over-performing the Pareto sample in every single objective function. Looking for the non-dominated samples, a set of optimal solutions is found, rather than a single one, whose samples are characterised by different trade-offs between the objectives and lay along a line going from low Mach and low velocity ratio (optimum samples according to the second objective function) to high Mach and high velocity ratio (optimum samples according to the first objective function). The samples where the entrance effects are still important are characterised by a high velocity ratio (*i.e.* a flatter velocity profile) compared to other samples having similar Mach numbers, thus resulting dominated: in the set there is at least one sample having both a larger Mach number and a lower velocity ratio. Removing from the full set of samples all those which are dominated in every single plot of Fig. 7, 700 samples are left. Fig. 8 is found by re-drawing Fig. 7 including only these samples.

Now the trends are much clearer, and the data can be interpolated in function of the Mach number, giving the needed $g(\mathrm{Ma})$ correlations. First of all, it can be noted that for $\mathrm{Ma} = 0$ the data intercept the incompressible correction terms already found in Section 4. Secondly, the derivatives with respect to the Mach number at $\mathrm{Ma} = 0$ are null. With the exception of the Poiseuille number, the correction terms shift towards unity without reaching it as the Mach number increases. It can be noted that the variations of the terms are more pronounced for the circular cross-section case, except for the Poiseuille number where the two lines grow in a similar fashion. All these considerations are in line with the expectations considering the flattening of the velocity profiles discussed in the previous section.

Following these observations, and also considering that the data spread is essentially null, polynomial functions with a given constant term and null linear term are deemed suitable for the data interpolation over the whole range of Mach numbers. The low interpolation errors that are found corroborate our hypothesis.

6.1. Circular cross-section channel

Concerning the circular cross-section channel, the data in Fig. 8 can be approximated by the following correlations. For the average velocity

$$U_{avg} = \left(\frac{1}{2} + 0.328\ \mathrm{Ma}^2 - 0.0939\ \mathrm{Ma}^3\right)\cdot U_{max}, \tag{61}$$

is found, while for the average dynamic pressure

$$p_{d,avg} = \left(\frac{4}{3} - 0.318\ \mathrm{Ma}^2 + 0.118\ \mathrm{Ma}^3\right)\cdot\frac{\rho_{blk}\,U_{avg}^2}{2}. \tag{62}$$

The bulk temperature varies with the Mach number as follows

$$T_{blk} = T_0 - (2 - 1.250\ \mathrm{Ma}^2 + 0.578\ \mathrm{Ma}^3)\cdot\frac{U_{avg}^2}{2c_{p,blk}}, \tag{63}$$

while for the friction factor

$$f = (1 + 0.653\ \mathrm{Ma}^2 + 2.809\ \mathrm{Ma}^3 - 5.311\ \mathrm{Ma}^4 + 4.157\ \mathrm{Ma}^5)\cdot\frac{64}{\mathrm{Re}} \tag{64}$$

holds. These formulas interpolate the numerical data with an average percent error $< 0.3\%$, with the exception of the latter whose average interpolation error is $< 0.5\%$.

6.2. Parallel-plates cross-section channel

The following correlations are found for the parallel-plates cross-section channel. For the average velocity we have

$$U_{avg} = \left(\frac{2}{3} + 0.0908\ \mathrm{Ma}^2 + 0.0487\ \mathrm{Ma}^3\right)\cdot U_{max}, \tag{65}$$

while for the average dynamic pressure

$$p_{d,avg} = \left(\frac{6}{5} - 0.0530\ \mathrm{Ma}^2 - 0.0524\ \mathrm{Ma}^3\right)\cdot\frac{\rho_{blk}\,U_{avg}^2}{2} \tag{66}$$

is found. For the bulk temperature

$$T_{blk} = T_0 - \left(\frac{54}{35} - 0.204\ \mathrm{Ma}^2 - 0.121\ \mathrm{Ma}^3\right)\cdot\frac{U_{avg}^2}{2c_{p,blk}}, \tag{67}$$

while for the friction factor

$$f = (1 + 0.153\ \mathrm{Ma}^2 + 2.632\ \mathrm{Ma}^3 - 4.685\ \mathrm{Ma}^4 + 3.669\ \mathrm{Ma}^5)\cdot\frac{96}{\mathrm{Re}} \tag{68}$$

holds. These formulas interpolate the numerical data with an average percent error $< 0.3\%$, with the exception of the latter whose average interpolation error is $< 0.5\%$.

Fig. 9 compares the friction factor correlation in Eq. (68) with previous correlations found in the literature for the parallel-plates cross-section channels. The given correlation is in line with the previous works, and is able to extend the prediction of f with confidence to Mach numbers up to 1, whereas the previous correlations were either validated only for low Mach numbers or were explicitly said to be unsuitable at higher Mach numbers.

7. Model validation

The correlations presented in Section 6 have been implemented in the one-dimensional Fanno flow numerical model developed. The model is then validated against two given channel geometries solved by means of CFD using Ansys Fluent: one having circular cross-section, the other with parallel-plates cross-section. The simulation setup is the same already discussed earlier. The channels are chosen with a high aspect ratio ($\alpha = 500$) in order to limit the role of the entrance effects as these are not modelled. Moreover, for a fair comparison, only the portion of channel not affected by the entrance effects is considered in the 1D simulation: the total pressure at a chosen section (*e.g.*, $50\,D_h$ from the inlet) is thus taken from CFD and imposed as upstream boundary condition of a $\alpha = 450$ channel solved with the one-dimensional model. Two different stagnation pressures are imposed in two simulations. The first is chosen so that the flow remains quasi-incompressible ($\mathrm{Ma} \leqslant 0.3$) throughout the channel, the second is chosen high enough so that the flow is choked. This allows the model predictive capability to be tested over the two extreme flow conditions. In particular, the second case corresponds to a configuration where the flow characteristics are difficult to be predicted, and where the standard Fanno models fail. A hydraulic diameter of $D_h = 40\,\mu\mathrm{m}$ and a downstream stagnation pressure $p_1 = 0.5$ bar are chosen so that laminar

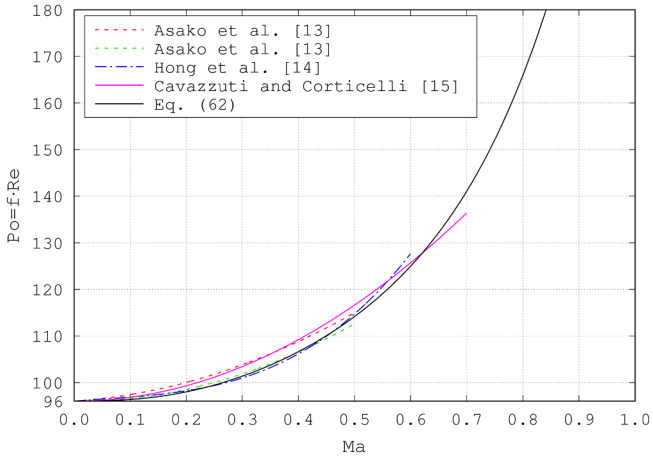

Fig. 9. Friction factor correlations for the case of laminar flow in parallel-plates cross-section channels: a comparison between the current and previous works in the literature.

flow is attained even with high upstream pressures.

A preliminary grid convergence test has been performed on the one-dimensional model for the four test cases. As an example, the results for the circular cross-section high Mach ($p_0 = 7.0$ bar) case are shown in Fig. 10 in terms of predicted mass flow rate. The 10^5 subdivisions grid has been chosen for validation purposes. This axial discretization grants a prediction error over the asymptotic value < 0.003%.

The results of the validation are shown in Table 3 and in Fig. 11. The CFD results are compared with the prediction of the enhanced model proposed and of the standard one-dimensional Fanno flow model. By the term standard we refer to the model where the correlations proposed in this work are not implemented, that is to say where all the terms within parenthesis in Eqs. (61)–(68) are substituted with 1. For brevity only the worst case scenario for what concerns the enhanced model predictions is reported in the figure (namely, the circular cross-section channel).

Table 3 reports values for some meaningful flow and calibration-related quantities sampled at a location reasonably close to the channel outlet. As we move closer to the outlet section, in fact, the predictive capability of the model worsens because of the increasing gradients with which the flow characteristics change, as shown in Fig. 11. This causes the minimum model prediction error to be amplified as we move downstream. Nonetheless, the enhanced Fanno flow model is able to report maximum prediction errors of about 1% at a longitudinal coordinate of $x/L = 0.9$ for the tested configurations. At the same location, with the standard model, the errors can grow by an order of magnitude and more.

Fig. 11 shows how the standard model is subject to significant errors, in particular for what concerns the prediction of the dynamic pressure, the temperature drop, and the friction factor. This translates into minor but yet significant errors in the prediction of pressures, Mach numbers, and all the other flow characteristics as the compressibility becomes important. On the other hand the enhanced model is able to replicate the CFD results very closely, proving the ability of the proposed correlations to enhance and extend the accuracy of the Fanno model predictions.

It is worth noting that, according to the CFD results, every quantity undergoes a sudden change at $x/L = 1$ which is not in line with the results that would reasonably be expected by looking at the figure. This is particularly evident for the friction factor (Fig. 11c) and when the Mach number approaches the sonic condition at the channel outlet (high p_0 configuration), and is to be ascribed to the change in the cross-section area encountered at this point (see also Fig. 3). The cross-section change is associated with an outlet pressure drop proportional to the square of the velocity, and induces changes in the velocity profile. Even though these changes may be small, the impact on the velocity gradient at the wall can be much larger, and this is why the friction factor appears to be more sensitive to this outlet effect. The CFD results are affected by this change in a close neighbourhood of the outlet section, as the flow settles to the downstream condition, inducing growths in the dynamic pressure, in the temperature drop, in the friction factor, and in the Mach number that locally can also become moderately larger than unity if the flow was already close enough to the choked condition. All this concurs to worsen the Fanno flow model predictions close to the outlet section, as can be seen in Fig. 11. These outlet effects in fact, even if marginal, are not accounted for in the one-dimensional model proposed.

8. Conclusions

An enhanced one-dimensional model for solving the Fanno flow problem is presented. Compared to the standard models that can be derived from the Fanno theory, a set of terms and functions are introduced for a better assessment of the dynamic pressure, the bulk temperature, and the friction factor in a quasi-2D fashion. The correction terms are firstly derived theoretically by analysing the velocity profiles predicted by the Poiseuille theory for the case of incompressible laminar flow in ducts of various cross-section shapes. Then, they are extended to the case of compressible laminar flow in terms of correlations calibrated on the basis of a set of 40 CFD simulations.

A detailed analysis of the velocity profiles and their dependence upon the Mach number allowed the correlations to be derived. The aim is to account for the effects due to the flow compressibility, also overcoming the intrinsic limitations of a one-dimensional model where all the flow-related quantities are represented, out of necessity, by a unique average value over the channel section.

The enhanced Fanno flow model has been validated over additional CFD simulations providing extremely good matchings for all the flow characteristics predicted when compared to a standard Fanno flow one-dimensional model. The proposed correlations, thus, allow to tackle the open question of the compressibility effects in micro-flows.

Other minor factors are known to influence the gas flow in micro-channels and still represent open challenges in the literature. Primarily we refer to the entrance effects promoting an extra friction in the entrance region of the channel where the velocity profiles are still far from being developed. As these effects are not addressed in the present work, their impact has been excluded by concentrating the current analysis far from this region. This allowed to isolate and better focus on the compressibility effects alone. Similarly, also exit effects have been pointed out by the CFD results, even though their impact has been shown to be marginal.

The numerical model presented provides an accurate predictive tool for modelling the micro-channel flow characteristics in laminar flows. Such a model can be used for the design of micro-channels in real-life applications, such as refrigeration systems, heat pumps, and MEMS, to cite a few. The model predictive capabilities remain very good also for Mach numbers approaching unity, that is where the traditional models fail in accounting for the compressibility effects properly.

Even though the model is based on the Fanno theory and as such is adiabatic, its extension in order to include heat transfer does not present particular challenges as long as the solution is carried out numerically as it is. Friction and heat flux, by modifying the local fluid density affect the velocity and are thus both responsible for the role of compressibility. By concentrating on the adiabatic flow it is possible to separate the effect of friction that would otherwise be confounded. This will also help in isolating the effects of heat flux in possible future works. The influence of heat flux on the velocity profiles and on compressibility could be the same as the one discussed here for friction, but not necessarily: the two effects could also sum up to give even flatter profiles. Nonetheless, in gas flows the impact of friction is expected to be larger than that the heat flux can achieve, and as such a better understanding of the role of friction is most relevant also for heat transfer applications. For instance, density reductions of a factor of 5–10 can be

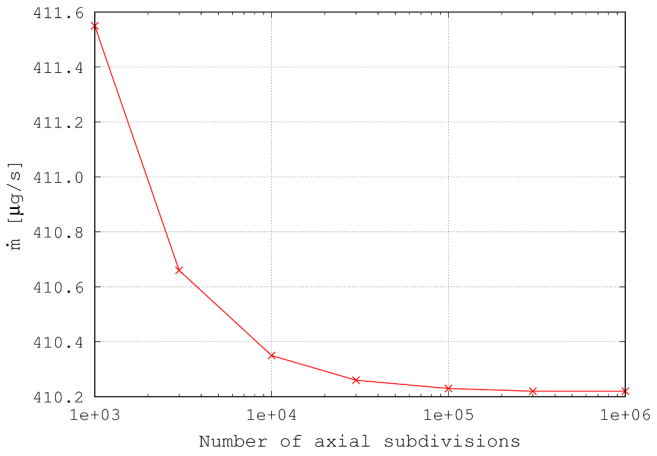

Fig. 10. One-dimensional model mesh convergence study.

Table 3
Model validation: CFD vs enhanced and standard one-dimensional Fanno flow model results. The values reported are those predicted at the longitudinal coordinate $x/L = 0.9$.

	$\dot{m}$ [μg/s]	p_d [kPa]	$T_0 - T_{blk}$ [K]	f	Ma
Circular cross-section channel, $p_0 = 2.7$ bar					
CFD	67.40	1.652	2.119	0.5595	0.1340
Enhanced	67.62 (+0.3%)	1.665 (+0.8%)	2.139 (+0.9%)	0.5563 (−0.6%)	0.1347 (+0.5%)
Standard	68.09 (+1.0%)	1.281 (−22%)	1.112 (−48%)	0.5447 (−2.6%)	0.1364 (+1.8%)
Circular cross-section channel, $p_0 = 7.0$ bar					
CFD	407.6	21.67	9.879	0.0979	0.2986
Enhanced	410.2 (+0.6%)	21.72 (+0.3%)	9.809 (−0.7%)	0.0971 (−0.8%)	0.2979 (−0.2%)
Standard	427.2 (+4.8%)	18.77 (−13%)	6.070 (−39%)	0.0857 (−13%)	0.3214 (+7.6%)
	$\dot{m}$ [mg/s]	p_d [kPa]	$T_0 - T_{blk}$ [K]	f	Ma
Parallel-plates cross-section channel, $p_0 = 3.4$ bar					
CFD	1.154	1.421	1.294	0.7733	0.1187
Enhanced	1.156 (+0.2%)	1.430 (+0.6%)	1.305 (+0.8%)	0.7699 (−0.4%)	0.1191 (+0.4%)
Standard	1.159 (+0.4%)	1.202 (−15%)	0.857 (−34%)	0.7647 (−1.1%)	0.1197 (+0.9%)
Parallel-plates cross-section channel, $p_0 = 13.7$ bar					
CFD	15.92	58.11	11.31	0.0589	0.3597
Enhanced	16.02 (+0.6%)	58.14 (+0.1%)	11.18 (−1.1%)	0.0583 (−0.9%)	0.3579 (−0.5%)
Standard	16.54 (+3.9%)	53.68 (−7.6%)	8.38 (−26%)	0.0525 (−11%)	0.3792 (+5.4%)

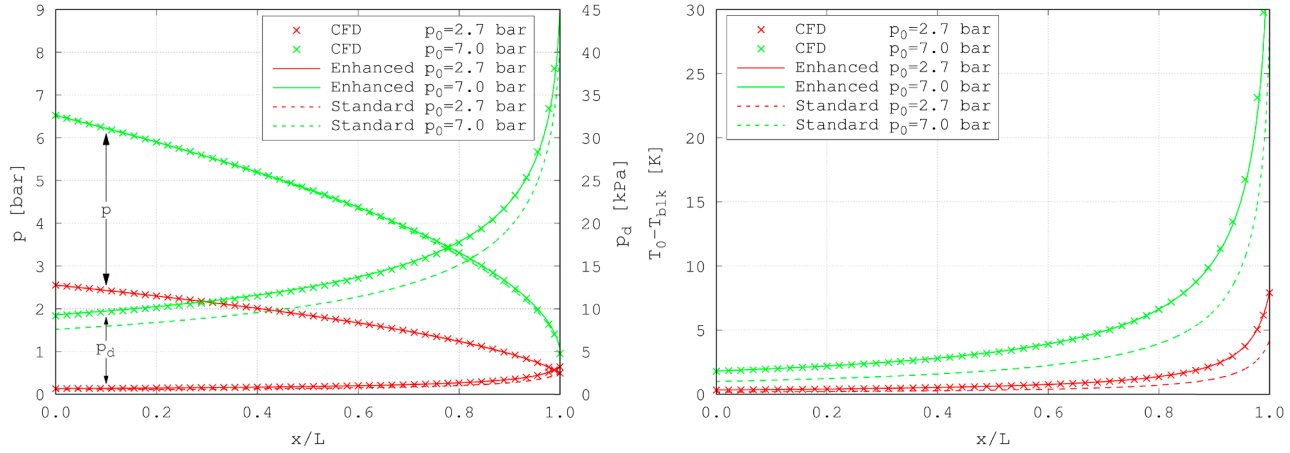

(a) Static and dynamic pressure

(b) Temperature drop

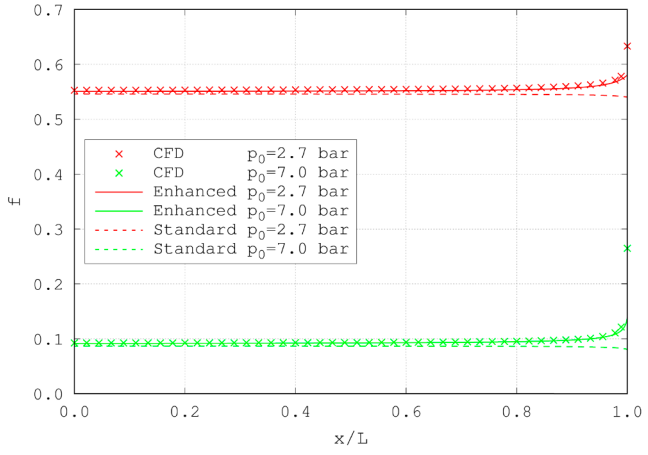

(c) Friction factor

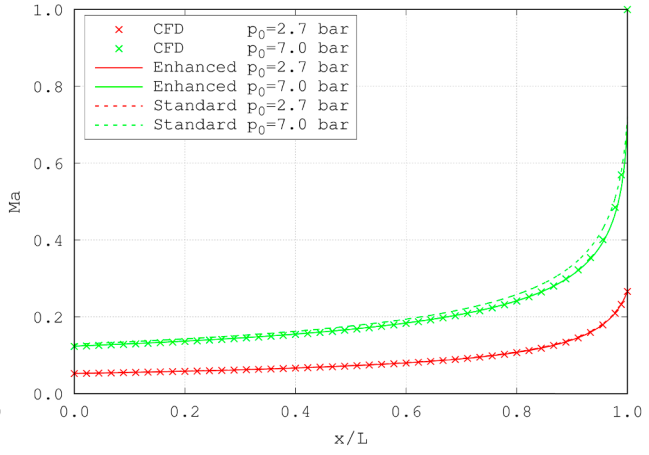

(d) Mach number

Fig. 11. Model validation: CFD vs enhanced and standard one-dimensional Fanno flow model results for the circular cross-section cases.

quite common in the crossing of a micro-channel. Considering the ideal gas state equation, this can be easily achieved with a pressure drop due to friction, but in most cases would require extremely high heat fluxes (approximately in the range of $10^5 \div 10^6$ W/m^2) to be obtained by means of temperature rise due to heating.

Conflict of interest statement

The authors certify that they have no affiliations with or involvement in any organization or entity with any financial interest or non-financial interest in the subject matter or materials discussed in this manuscript.

References

[1] M.J. Moran, H.N. Shapiro, D.D. Boettner, M. Bailey, Fundamentals of Engineering Thermodynamics, seveth ed., John Wiley & Sons, 2010.
[2] P. Rosa, T.G. Karayiannis, M.W. Collins, Single-phase heat transfer in micro-channels: the importance of scaling effects, Appl. Therm. Eng. 29 (2009) 3447–3468.
[3] S.D. Deodhar, H.B. Kothadia, K.N. Iyer, S.V. Prabhu, Experimental and numerical studies of choked flow through adiabatic and diabatic capillary tubes, Appl. Therm. Eng. 90 (2015) 879–894.
[4] N.S. Kumar, K.T. Ooi, One dimensional model of an ejector with special attention to Fanno flow within the mixing chamber, Appl. Therm. Eng. 65 (1) (2014) 226–235.
[5] N. Agrawal, S. Bhattacharyya, Adiabatic capillary tube flow of carbon dioxide in a transcritical heat pump cycle, Int. J. Energy Res. 31 (2007) 1016–1030.
[6] G.P. Mignot, M.H. Anderson, M.L. Corradini, Measurement of supercritical CO2 critical flow: effects of L/D and surface roughness, Nucl. Eng. Des. 239 (5) (2009) 949–955.
[7] M. Cioffi, E. Puppo, A. Silingardi, Fanno design of blow-off lines in heavy duty gas turbine, Proceedings of ASME Turbo Expo 2013, San Antonio, Texas, USA, June 3rd-7th, 2013.
[8] W.J. Kostowski, J. Skorek, Real gas flow simulation in damaged distribution pipelines, Energy 45 (2012) 481–488.
[9] J.-S. Plante, J. Vogan, T. El-Aguizy, A.H. Slocum, A design model for circular porous air bearings using the 1D generalized flow method, Precision Eng. 29 (3) (2005) 336–346.
[10] T. Shiraishi, E. Murayama, Y. Kawakami, K. Nakano, Approximate simulation of pneumatic steady flow characteristics in tubes with friction, Proceedings of the 8th JFPS International Symposium on Fluid Power, pages 242–247, Okinawa, October 25th-28th, 2011.
[11] D. Kawashima, Y. Asako, Data reduction of friction factor of compressible flow in micro-channels, Int. J. Heat Mass Transf. 77 (2014) 257–261.
[12] M.J. Kohl, S.I. Abdel-Khalik, S.M. Jeter, D.L. Sadowski, An experimental investigation of microchannel flow with internal pressure measurements, Int. J. Heat Mass Transf. 48 (8) (2005) 1518–1533.
[13] Y. Asako, T. Pi, S.E. Turner, M. Faghri, Effect of compressibility on gaseous flows in micro-channels, Int. J. Heat Mass Transf. 46 (16) (2003) 3041–3050.
[14] C. Hong, T. Nakamura, Y. Asako, I. Ueno, Semi-local friction factor of turbulent gas flow through rectangular microchannels, Int. J. Heat Mass Transf. 98 (2016) 643–649.
[15] M. Cavazzuti, M.A. Corticelli, Numerical modelling of Fanno flows in micro channels: a quasi-static application to air vents for plastic moulding, Therm. Sci. Eng. Progr. 2 (2017) 43–56.
[16] X.K. Kakatsioss, G.E. Houzouris, H.S. Giannakopoulou, Accurate solutions and empirical relations for inviscid-diabatic and viscous-adiabatic one-dimensional flows of real steam, Energy Convers. Manage. 39 (12) (1998) 1277–1288.
[17] D. Stojkovic, V.D. Djordjevic, P.S. Cvijanovic, On the effect of friction in steady flow of dense gases in pipes, Int. J. Heat Fluid Flow 22 (4) (2001) 480–485.
[18] I.B. Sebastião, W.F.N. Santos, Gas-surface interaction effects on the flowfield structure of a high speed microchannel flow, Appl. Therm. Eng. 52 (2013) 566–575.
[19] Q. You, I. Hassan, Experimental investigation on flow boiling instability in a microtube with and without an inlet orifice in vertical flow directions, Therm. Sci. Eng. Progr. 4 (2017) 18–29.
[20] W.H.T. Loh, A generalized one-dimensional compressible flow analysis with heat addition and/or friction in a non-constant area duct, Int. J. Eng. Sci. 8 (3) (1970) 193–206.
[21] G.J. Parker, Adiabatic compressible flow in parallel ducts: an approximate but rapid method of solution, Int. J. Heat Fluid Flow 10 (2) (1989) 179–181.
[22] E. Urata, A flow rate equation for subsonic Fanno flow, Proc. Inst. Mech. Eng., Part C: J. Mech. Eng. Sci. 227 (12) (2013) 2724–2729.
[23] D. Ngomo, A. Chaudhuri, A. Chinnayya, A. Hadjadj, Numerical study of shock propagation and attenuation in narrow tubes including friction and heat losses, Comput. Fluids 39 (2010) 1711–1721.
[24] G.L. Morini. The challenge to measure single-phase convective heat transfer coefficients in microchannels. Heat Transfer Engineering, In press, published online on march 15th 2018.
[25] G. Hetsroni, A. Mosyak, E. Pogrebnyak, L.P. Yarin, Fluid flow in micro-channels, Int. J. Heat Mass Transf. 48 (10) (2005) 1982–1998.
[26] R.K. Shah, A.L. London, Laminar Flow Forced Convection in Ducts: A Source Book for Compact Heat Exchanger Analytical Data, Academic Press, 1978.
[27] M.A. Al-Nimr, V.A. Hammoudeh, M.A. Hamdan, M.H. Es-Saheb, Fanno flow in microchannels, Res. J. Appl. Sci., Eng. Technol. 4 (24) (2012) 5578–5585.
[28] M.R.S. Bushehri, H. Ramin, M.R. Salimpour, A new coupling method for slip-flow and conjugate heat transfer in a parallel plate micro heat sink, Int. J. Therm. Sci. 89 (2015) 174–184.
[29] C. Hong, Y. Asako, J.-H. Lee, Heat transfer characteristics of gaseous flows in microchannel with constant heat flux, Int. J. Therm. Sci. 46 (2007) 1153–1162.
[30] J.D. Anderson, Modern Compressible Flow: With Historical Perspective, McGraw-Hill, 1990.
[31] W. Sutherland. LII. The viscosity of gases and molecular force. The London, Edinburgh, and Dublin Philosophical Magazine and Journal of Science, 36(223), 507–531, 1893.
[32] M.W. Chase, JANAF Thermochemical Tables, National Bureau of Standards, 1985.
[33] J. Boussinesq, Mémoire sur l'influence des frottements dans les mouvements réguliers des fluids, J. Math. Pures Appl. 13 (21) (1868) 377–424.
[34] V. Pareto, Manuale di economia politica con una introduzione alla scienza sociale, Societá Editrice Libraia (1906).
[35] M. Reyes-Serra, C.A. Coello Coello, Multi-objective particle swarm optimizers: a survey of the state-of-the-art, Int. J. Comput. Intell. Res. 2 (3) (2006) 287–308.
[36] M. Cavazzuti, Optimization Methods: From Theory to Design. Scientific and Technological Aspects in Mechanics, Springer, 2013.